Supporting information

L-Methionine modified active ice enables ultra-rapid methane hydrate kinetics for solidified natural gas storage

Yang Li,[a] Jibao Zhang,[a] Jingbo Gao,[a] Guangjin Chen[b] and Zhenyuan Yin*[a]

[a] Institute for Ocean Engineering, Shenzhen International Graduate School, Tsinghua University, Shenzhen 518055, China

[b] State Key Laboratory of Heavy Oil Processing, China University of Petroleum, Beijing 102249, China

* Corresponding author: zyyin@sz.tsinghua.edu.cn (Z. Yin)

Number of pages: 46

Number of sections: 6

Number of figures: 33

Number of tables: 7

Section 1. Methodology and data processing for *in-situ* Raman Spectroscopy

1.1 Schematic diagram of the Raman probe position in the non-visualized reactor

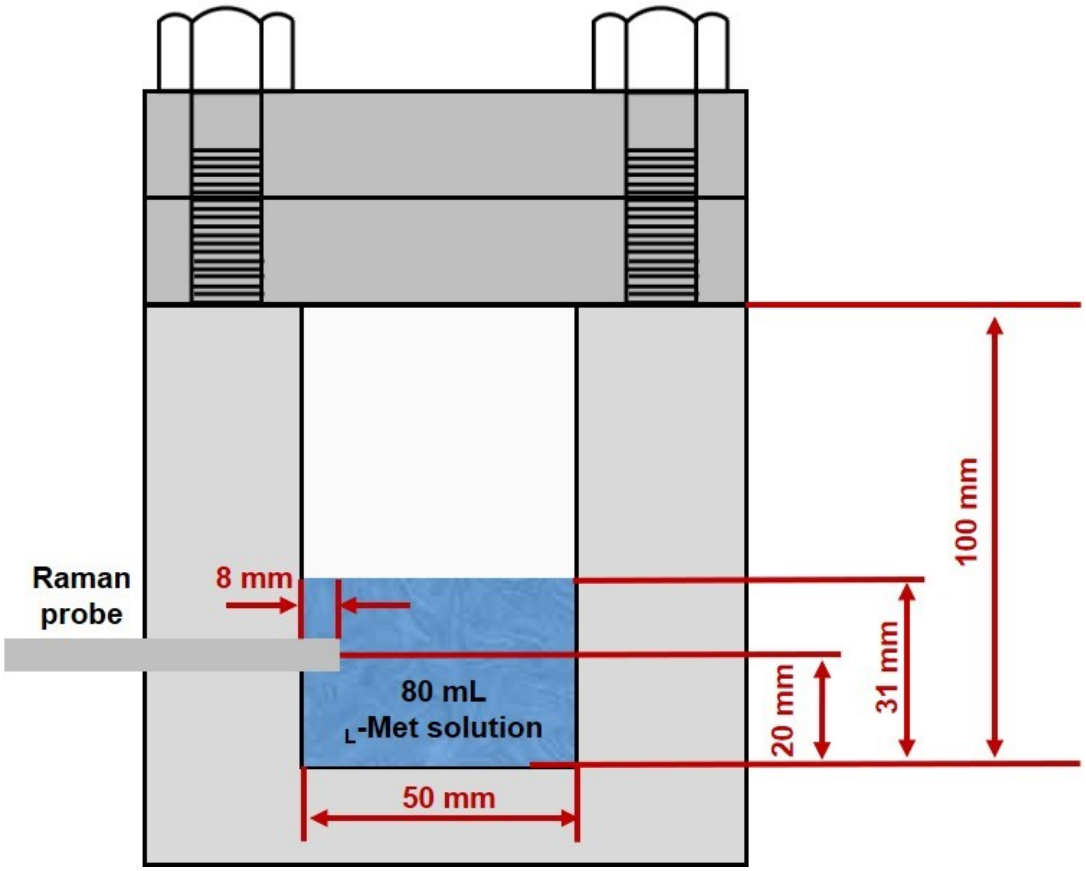

Fig. S1. Schematic diagram showing the position of the Raman probe in the non-visualized reactor.

1.2 Measured Raman peak for different CH_4 states

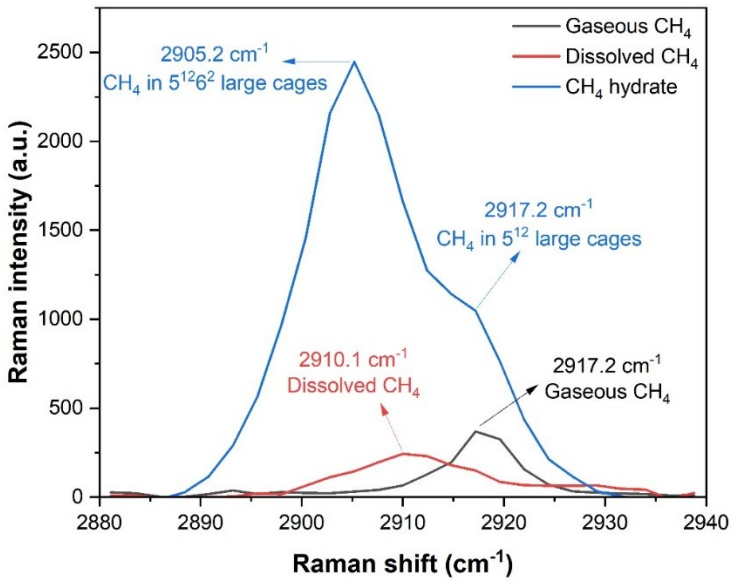

Fig. S2. Raman spectroscopy of gaseous CH_4 in different states, showing the characteristic peaks of gaseous (black curve), dissolved (red curve), and CH_4 hydrate (blue curve) in the 2880-2940 cm^{-1} region.

To better analyze the Raman spectra of CH_4 hydrate formation, we first obtained Raman spectra of gaseous CH_4, dissolved CH_4, and CH_4 hydrate. Fig. S2 and Table S1 present the comparison of the obtained Raman spectra, which can be differentiated from each other based on the specific vibrational frequencies. The Raman band at 2910.1 cm^{-1} corresponds to dissolved CH_4, while gaseous CH_4 exhibits a peak at 2917.2 cm^{-1}. For CH_4 hydrate, the characteristic bands are observed at 2905.2 cm^{-1} and 2917.2 cm^{-1}, assigned to CH_4 molecules enclathrated in $5^{12}6^2$ large cages and 5^{12} small cages, respectively.[1]

Table S1. Measured Raman shift of CH_4 in the gaseous phase, dissolved phase and hydrate phase in this work.

Phase	Raman shift (cm^{-1})	
Gaseous CH_4	2917.2	
Dissolved CH_4	2910.1	
CH_4 hydrate	$5^{12}6^2$ large cages	5^{12} small cages
	2905.2	2917.2

1.3 Temperature and pressure evolution during CH_4 hydrate formation from 0.3 wt% $_L$-Met modified active ice in the *in-situ* Raman characterization experiments

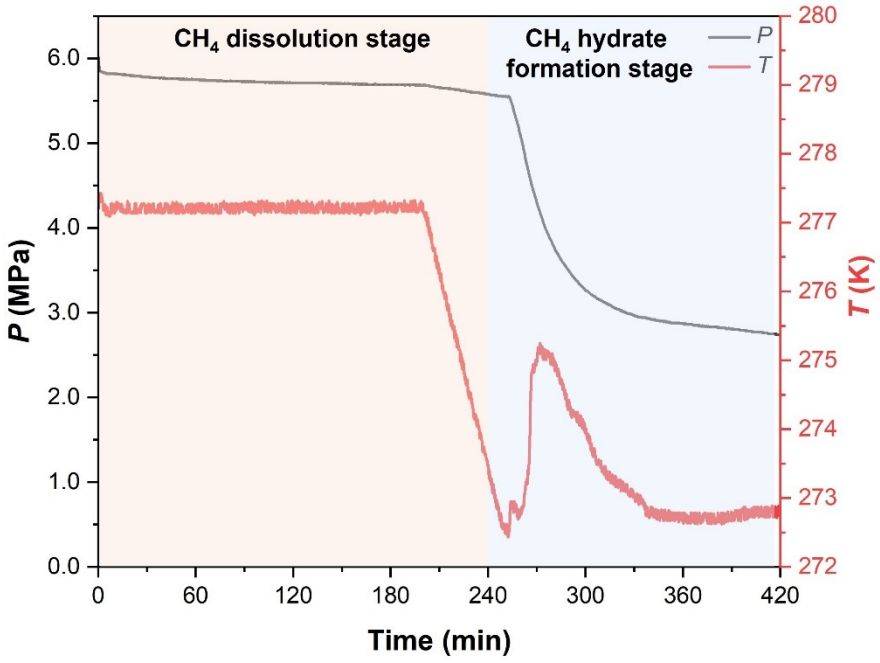

Fig. S3. Temperature-pressure (*P*-*T*) evolution corresponding to the *in-situ* Raman measurements during CH_4 hydrate formation from 0.3 wt% $_L$-Met solution at P = 6.0 MPa, T = 277.2 K (1st formation stage) and subsequent T = 272.7 K (2nd formation stage).

1.4 Measured Raman spectra for gaseous CH_4 under different pressures

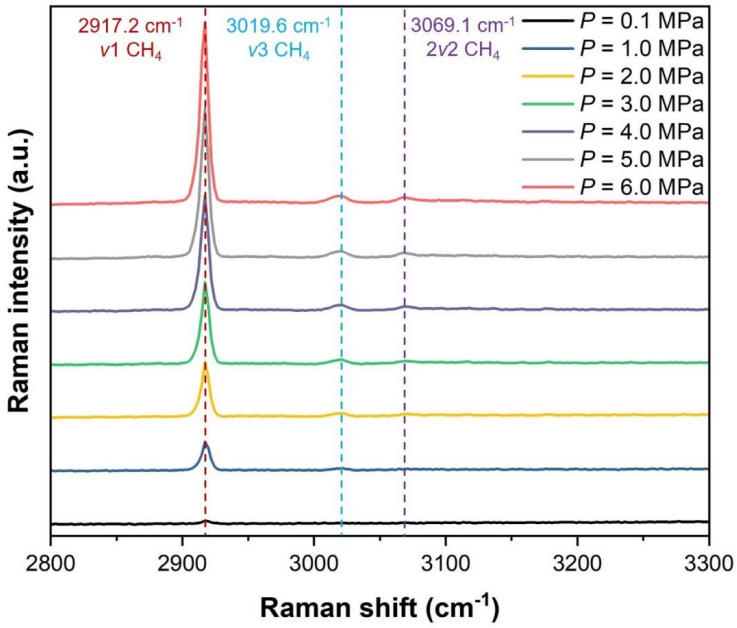

Fig. S4. Raman spectroscopy of gaseous CH_4 under different pressures (0.1–6.0 MPa), showing peaks in the 2800–3300 cm^{-1} range.

Fig. S4 shows the Raman spectroscopy of gaseous CH_4 under different pressures. After purging three times, the Raman peak at 2917.2 cm^{-1}, corresponding to the v_1 vibrational mode of CH_4, remained clearly observable even at ambient pressure of 0.1 MPa. When the pressure increased to 1.0 MPa, the intensity of this main peak was significantly enhanced, accompanied by the emergence of two additional peaks at 3019.6 cm^{-1} (v_3 mode) and 3069.1 cm^{-1} ($2v_2$ overtone), corresponding specifically to the v_3 and $2v_2$ vibrations of CH_4, respectively, as summarized in Table S2. Together, these Raman peaks provide a clear signature of gaseous CH_4. As the pressure continued to rise, the intensities of all characteristic peaks systematically increased. At the same time, their positions and spectral shapes remained essentially unchanged, indicating that CH_4 remained in the gas phase throughout the studied pressure range.

Table S2. Assignment of Raman shifts for CH_4 vibrational modes (cm^{-1}) with corresponding shorthand notation and vibrational description.[2]

Raman shift (cm^{-1})	bending vibrational mode	
~2576	C-H overtone of the symmetric bending band	$2v_4$
~2917	C-H symmetric stretching band	v_1
~3006	C-H asymmetric stretching band	v_3
~3070	C-H overtone of the asymmetric bending band	$2v_2$

1.5 Pressure and temperature evolution during 0.3 wt% $_L$-Met modified active ice synthesis in the *in-situ* Raman characterization experiments

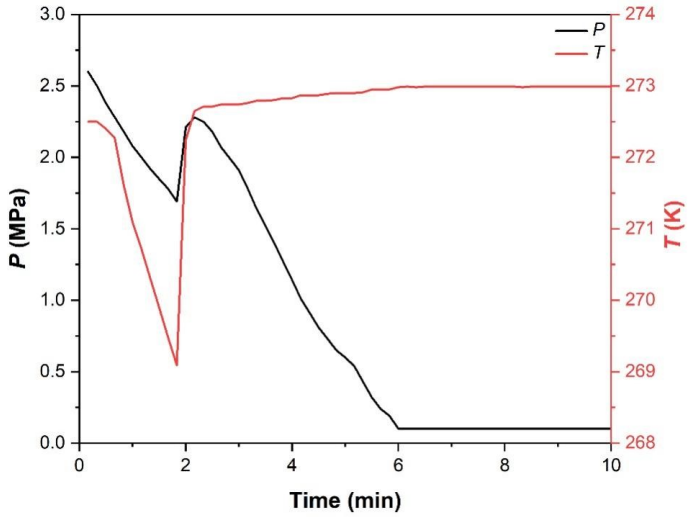

Fig. S5. Temperature-pressure (*P*-*T*) evolution during the first 10 min corresponding to the *in-situ* Raman experiment during the CH_4 hydrate dissociation to form $_L$-Met modified active ice at P = 0.1 MPa and T = 272.7 K.

1.6 *In-situ* Raman spectroscopy of CH_4 hydrate formation from 0.3 wt% $_L$-Met modified active ice

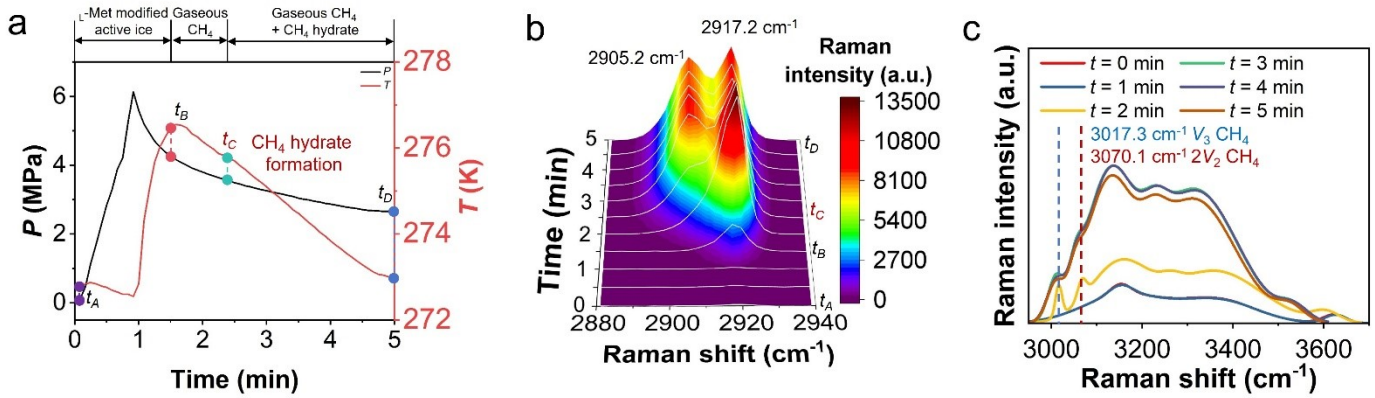

Fig. S6. (a) Pressure-temperature (*P*-*T*) evolution corresponding to the *in-situ* Raman experiment during the CH_4 hydrate formation from the $_L$-Met modified active ice (P = 6.0 MPa, T = 272.7 K); (b) time-dependent *in-situ* Raman spectroscopy showing CH_4 Raman peaks evolution at 2880–2940 cm^{-1} and (c) water Raman peaks evolution at 2940–3700 cm^{-1}.

1.7 Gaussian fitting methodology for deconvoluting Raman spectra

To minimize subjectivity and ensure robustness, we established a rigorous, four-step standardized protocol for the spectral deconvolution (illustrated using the 0.3 wt% $_L$-Met modified active system at t = 5 min):

i) Range selection: We consistently analyzed the 2940-3700 cm^{-1} range, which encompasses the O-H stretching vibrations characterizing the hydrogen-bond network (see Fig. S7).

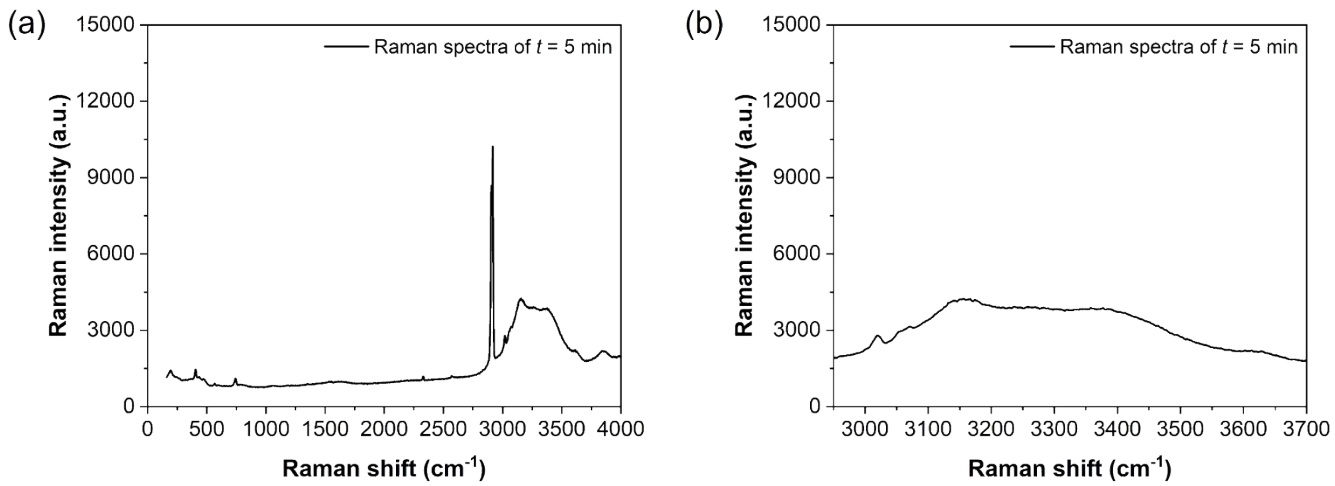

Fig. S7. Raman spectra acquired during CH_4 hydrate formation from 0.3 wt% $_L$-Met modified active ice at t = 5 min: (a) full spectrum from 0 to 4000 cm^{-1}; (b) Magnified view of the O-H of water and C-H stretching of CH_4 region (2950-3700 cm^{-1}).

ii) Baseline correction: A linear baseline was anchored at the minima (2940 cm^{-1} and 3700 cm^{-1}) and subtracted to eliminate background offsets uniformly across all samples (see Fig. S8).

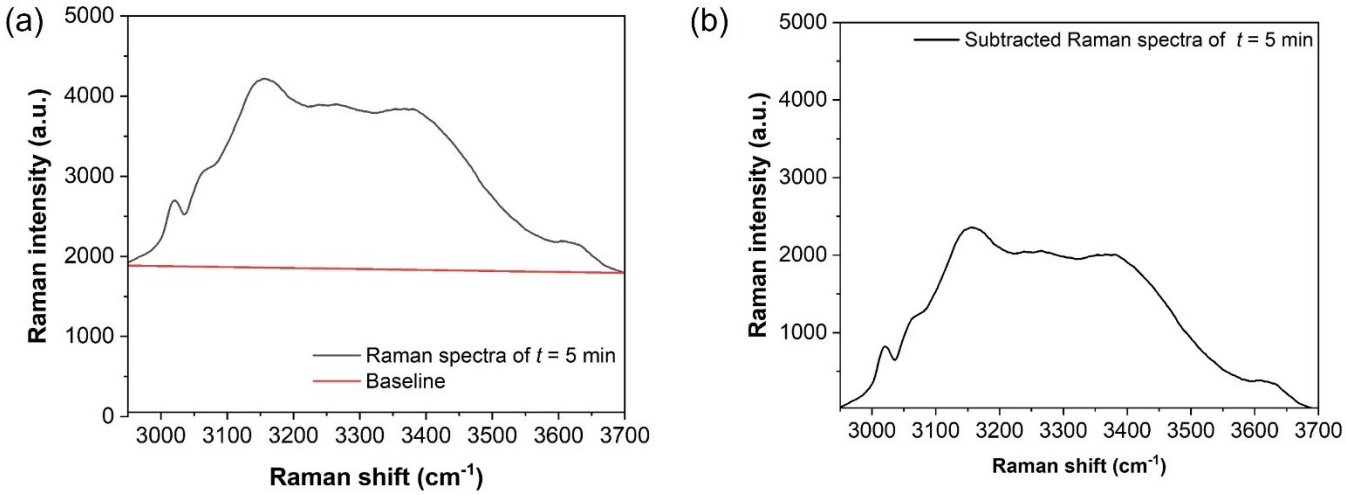

Fig. S8. Raman spectral baseline correction for CH_4 hydrate formation from 0.3 wt% $_L$-Met modified active ice at t = 5 min: (a) original spectrum with fitted baseline; (b) baseline-subtracted spectrum.

iii) Peak initialization and Optimization and quantification: After baseline correction, Gaussian peaks were initialized for both the O-H stretching region and CH_4 vibration modes based on literature-reported values, ensuring the physical validity of the deconvolution model (see Fig. S9). In Raman spectroscopy, the Gaussian fitting function is commonly expressed as:

$$y(x) = \sum_{i=1}^{n} [A_i \times e^{-\frac{(x-\mu_i)^2}{2\sigma_i^2}}] + B \quad (1)$$

where n, A_i, μ_i, σ_i, and B represent Number of peaks, Amplitude, center, standard deviation of the i-th peak, and global baseline constant, respectively.

The fitting parameters were then iteratively optimized to maximize statistical accuracy. After 66 optimization cycles, the goodness of fit improved from R^2 = 0.96 to R^2 = 0.99. Based on this optimized fit, we

obtained integrated areas I_{DDAA} = 2032.9 and I_{DA} = 2008.9, yielding a final ratio of $I_{DDAA/DA}$ = 1.02. This consistent strategy was applied to all samples to quantify the proportion of strong vs. weak hydrogen bonds.

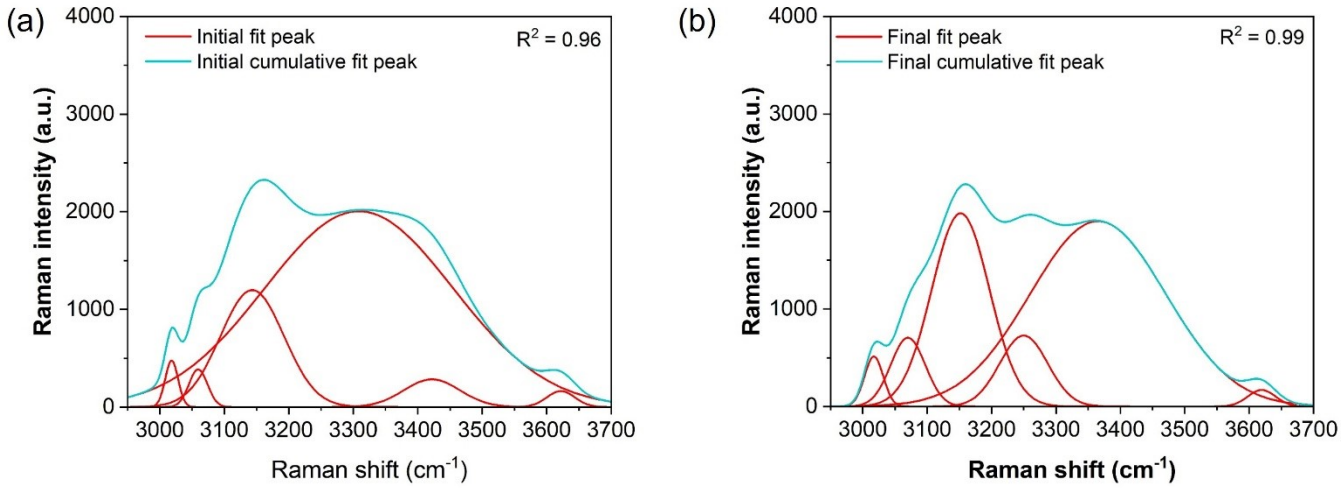

Fig. S9. Gaussian fitting optimization process for the O-H stretching Raman band: (a) initial peak fitting result before optimization (R^2 = 0.96); (b) final peak fitting result after 66 optimization iterations (R^2 = 0.99).

(3) Sensitivity analysis: To explicitly validate the robustness of the calculated $I_{DDAA/DA}$ ratio, we performed a systematic sensitivity analysis. Starting from the optimized benchmark value of $I_{DDAA/DA}$ = 1.02 (base Case 1), we evaluated the impact of methodological perturbations through two distinct scenarios. Vertically shifting the baseline by +100 intensity (Case 2) counts yielded a ratio of 1.04. Unconstrained Fitting: Relaxing the rigid constraints on peak positions during the Gaussian fitting process (Case 3) resulted in a ratio of 1.01 (see Fig. S10). In both cases, the relative deviation from the benchmark was less than 2%. This minimal variation confirms that the $I_{DDAA/DA}$ metric is mathematically robust and insensitive to minor fluctuations in baseline selection or fitting constraints.

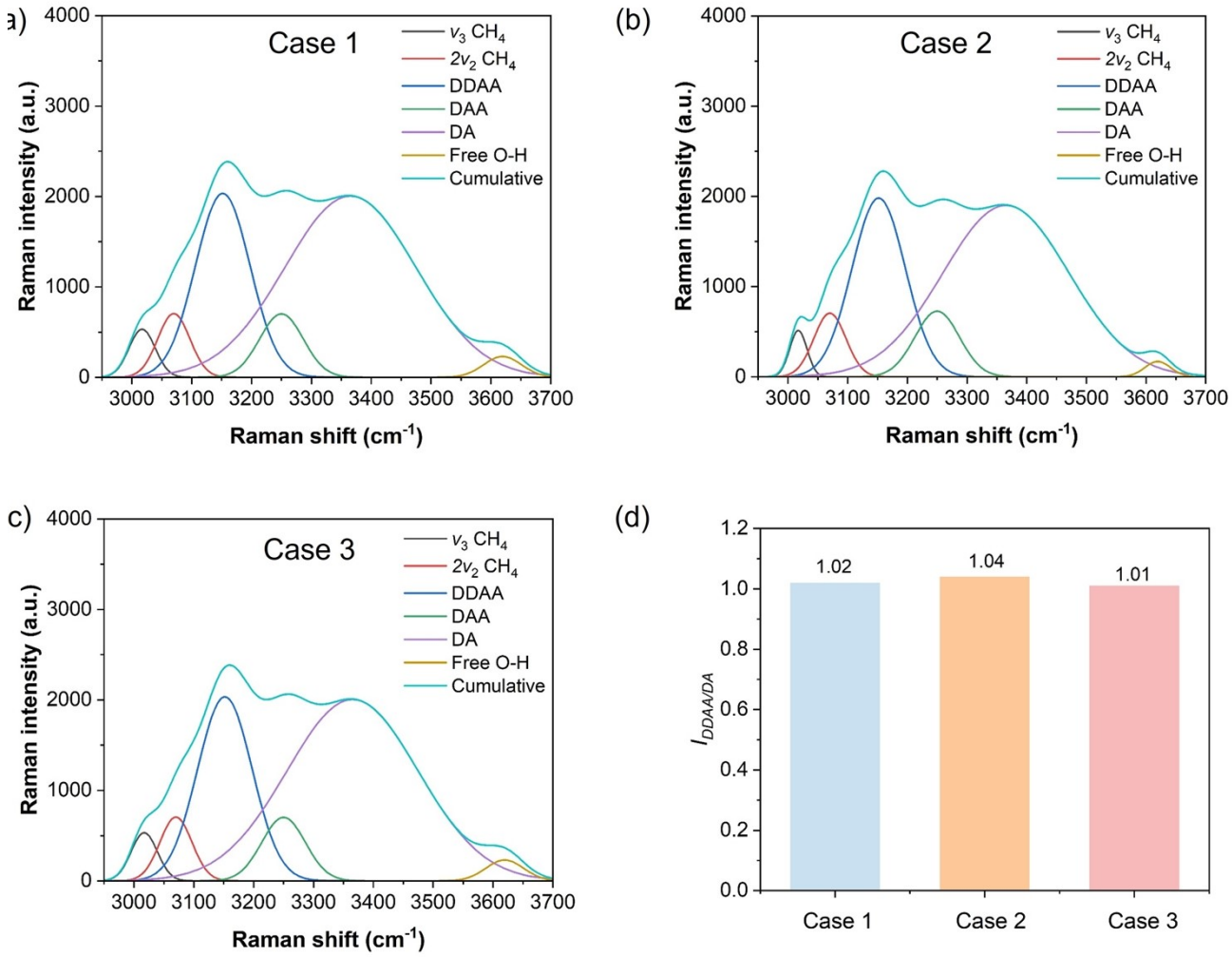

Fig. S10. Sensitivity analysis of the hydrogen bond ordering ($I_{DDAA/DA}$) to data processing methods: (a) baseline scenario; (b) with altered baseline correction; (c) without fixed peak positions; and (d) direct comparison of the resulting $I_{DDAA/DA}$ values across the three cases.

1.8 Deconvolution of Raman spectroscopy by Gaussian fitting to identify gaseous CH_4 and CH_4 hydrate

Owing to the intrinsic proximity of the vibrational modes, the band at approximately 2917.2 cm^{-1} represents a superimposed signal that may originate from free gaseous CH_4, CH_4 encaged in the 5^{12} small cages, or the coexistence of both species. To ensure a physically meaningful deconvolution, we first identified the gaseous CH_4 using independent and unambiguous spectral markers before performing peak fitting. Specifically, the presence of gaseous CH_4 was confirmed by its characteristic overtone and stretching vibrations at 3070.1 cm^{-1} ($2\nu_2$) and 3071.3 cm^{-1} (ν_3), while the formation of the CH_4 hydrate phase was

explicitly identified by the characteristic vibration of CH_4 in the $5^{12}6^2$ large cages at 2905.2 cm^{-1}, as shown in Fig. S11.

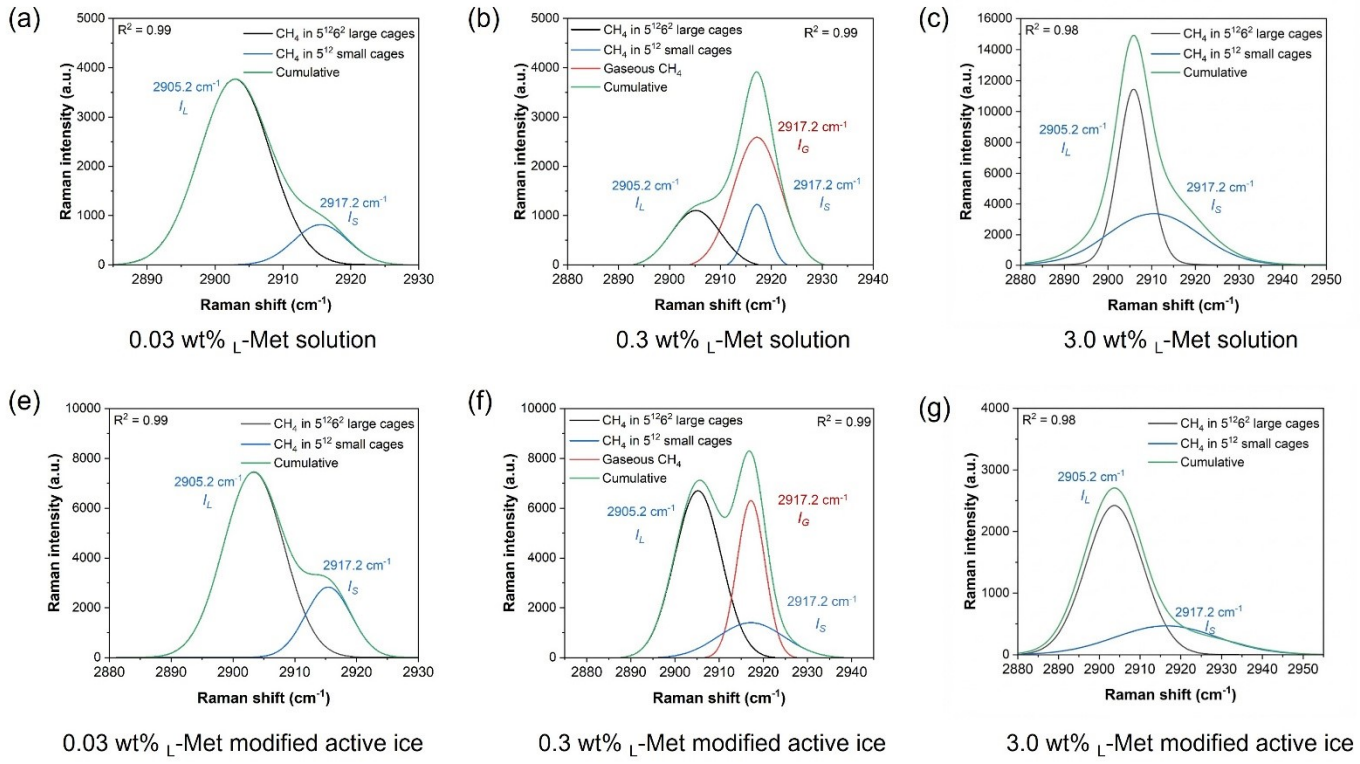

Fig. S11. Gaussian fitting results of Raman spectra for CH_4 hydrates formed in different systems: (a)-(c): 0.03-3.0 wt% $_L$-Met solution system and (e)-(g): 0.03-3.0 wt% $_L$-Met modified active ice system.

1.9. Gaussian fitting results of water Raman peaks in 0.3 wt% $_{L}$-Met solution

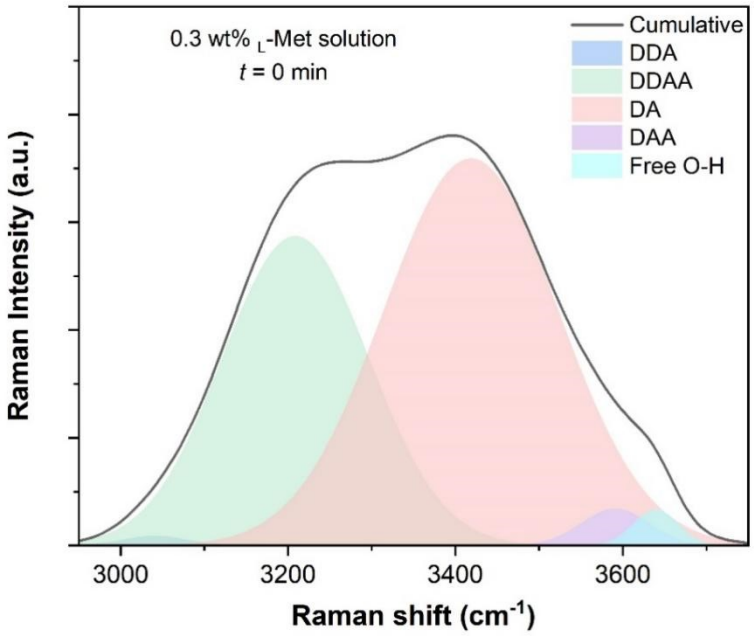

Fig. S12. Gaussian fitting of O-H stretching peak in 0.3 wt% $_{L}$-Met solution.

Based on the Gaussian fitting of the O-H stretching band in the Raman spectrum for the 0.3 wt% $_{L}$-Met solution at t = 0 min, the initial hydrogen-bond network was quantitatively resolved into five distinct configurations: DDAA (double donor–double acceptor), DDA (double donor–single acceptor), DAA (single donor–double acceptor), DA (single donor–single acceptor), and non-hydrogen-bonded free O-H species (see Fig. S9 and Table S3). The ratio of $I_{DDAA/DA}$ was used to evaluate the hydrogen-bond ordering degree, reflecting the relative abundance of fully tetrahedral versus distorted hydrogen-bond structures.[3,4]

Table S3. Gaussian-fitted Raman shifts of water O–H stretching vibrational sub-bands (DAA, DDAA, DA, DDA, Free O–H) and $2\nu_2$ CH_4 mode in different states (0.3 wt% $_L$-Met solution, initial CH_4 hydrate formation from 0.3 wt% $_L$-Met solution, $_L$-Met modified active ice, and subsequent CH_4 hydrate formation from 0.3 wt% $_L$-Met modified active ice).

System	Raman shift (cm^{-1})					
	DAA	$2\nu_2$ CH_4	DDAA	DA	DDA	Free O-H
0.3 wt% $_L$-Met solution	3039.1	—	3206.9	3417.1	3586.6	3640.1
Initial CH_4 hydrate	3040.2	3069.7	3207.3	3417.1	3591.2	3638.9
Active ice	3152.6	—	3152.6	3367.1	3270.3	3621.2
Subsequent CH_4 hydrate	3017.2	3070.1	3151.9	3365.2	3268.5	3619.5

1.10 Calculation of cage occupancy and hydration number of CH_4 hydrate formed in $_L$-Met solution and active ice systems

The cage occupancy and hydration numbers (*Nh*) were calculated for both the $_L$-Met solution system and the $_L$-Met modified active ice system under different $_L$-Met concentrations, based on Raman spectroscopic characterization combined with the van der Waals-Platteeuw (vdW-P) thermodynamic model.

For sI hydrate, the ideal stoichiometric ratio of 5^{12} small cages to $5^{12}6^2$ large cages is 1:3. Accordingly, the relative cage occupancy can be calculated using Equation (1):

$$\frac{\theta_S}{\theta_L} = \frac{3I_S}{I_L} \tag{2}$$

Where θ_S and θ_L represent the relative occupancies of CH_4 in the 5^{12} small cages and $5^{12}6^2$ large cages, respectively. I_S and I_L represent the corresponding Raman peak intensities of CH_4 in the hydrate phase. Further quantitative analysis of cage occupancy can be conducted based on the van der Waals-Platteeuw (vdW-P) statistical thermodynamic model. For sI hydrates, the chemical potential of water molecules in the hydrate lattice can be expressed by Equations (2) and (3):

$$\mu_W(h)-\mu_W(h^0) = \frac{RT}{23}[3\ln(1-\theta_L)+\ln(1-\theta_S)] \quad (3)$$

$$\mu_W(h)-\mu_W(h^0) = -\Delta\mu_W^0 \quad (4)$$

$\mu_w(h)$ is the chemical potential of water molecules in the hydrate phase, and $\mu_w(h^0)$ is that of water in the empty hydrate lattice. R is the universal gas constant, and T is the formation temperature of the CH_4 hydrate. Under equilibrium conditions, the chemical potential difference $\Delta\mu 0\ W$ between water in the hydrate phase and the free water phase for sI hydrates is approximately 1297 J/mol. Then, the hydration number (N_H) can be calculated based on Equation (4):

$$n_H = \frac{23}{3\theta_L + \theta_S} \quad (5)$$

The calculated cage occupancies and hydration numbers of CH_4 hydrate are presented in Fig. S17 and Table S4. The results show that the large cage occupancy (θ_L) remained consistently high across all systems, exceeding 96%, which indicates that the large cages were nearly fully occupied by CH_4 molecules regardless of the $_L$-Met concentration or the system type ($_L$-Met solution and $_L$-Met modified active ice). However, the small cage occupancy (θ_S) showed distinct behaviours. In the $_L$-Met solution system, θ_S increased from 82.01% to 90.79% with increasing $_L$-Met concentration. Conversely, in the modified active ice system, θ_S started at 87.98% at 3.0 wt%. Most notably, the calculated hydration numbers (N_H) for all synthesized hydrates ranged between 5.98 and 6.17. These values are highly consistent with the theoretical value of 6.0 for ideal structure I (sI) CH_4 hydrate, suggesting high structural integrity of the formed hydrates. In the $_L$-Met solution systems, the small cage occupancy θ_S did not show a clear trend with increasing promoter concentration, whereas in the modified active ice systems, θ_S gradually decreased with increasing $_L$-Met concentration.

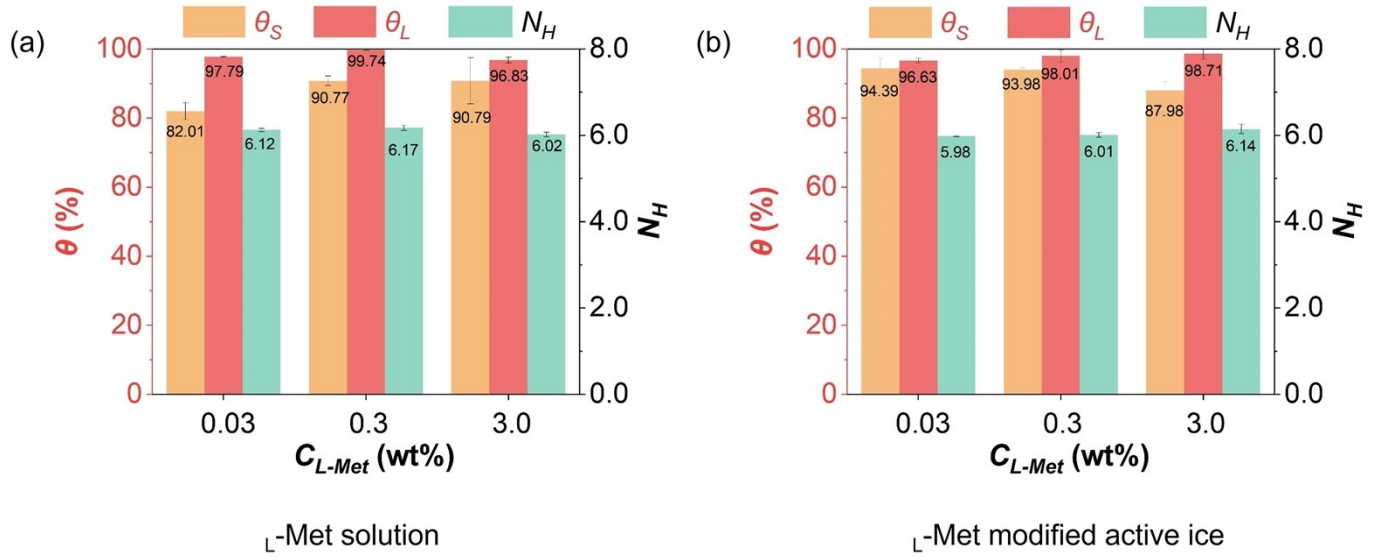

$_L$-Met solution

$_L$-Met modified active ice

Fig. S13. illustrates the cage occupancy and hydration numbers of CH_4 hydrate calculated from the Raman spectral results: (a) $_L$-Met solution system and (b) $_L$-Met modified active ice system.

For the $_L$-Met solution hydrate system, the calculated hydration numbers vary from 6.02 to 6.17, with an average value of 6.10. For the $_L$-Met modified active ice system, the hydration numbers range from 5.98 to 6.14, with an average value of 6.04 (see Fig. S13 and Table S4). These results indicate that the hydration numbers for both systems are close to the theoretical value of 6.0 for sI CH_4 hydrate, with only minor variations arising from experimental conditions and local structural heterogeneity.

To assess the influence of hydration number selection on the calculated CH_4 storage capacity, a sensitivity analysis was performed using the maximum hydration numbers obtained from Raman analysis. For the solution system, methane storage capacities calculated using N_H = 6.17 and N_H = 6.0 are 156.9 V_g/V_w and 160.1 V_g/V_w, respectively, corresponding to a deviation of approximately 2.0% (see Fig. S14). Similarly, for the $_L$-Met modified active ice system, the calculated methane storage capacities are 161.8 V_g/V_w (N_h = 6.14) and 164.5 V_g/V_w (N_h = 6.0), yielding a deviation of about 1.7%. These differences are relatively small and well within acceptable experimental uncertainty.

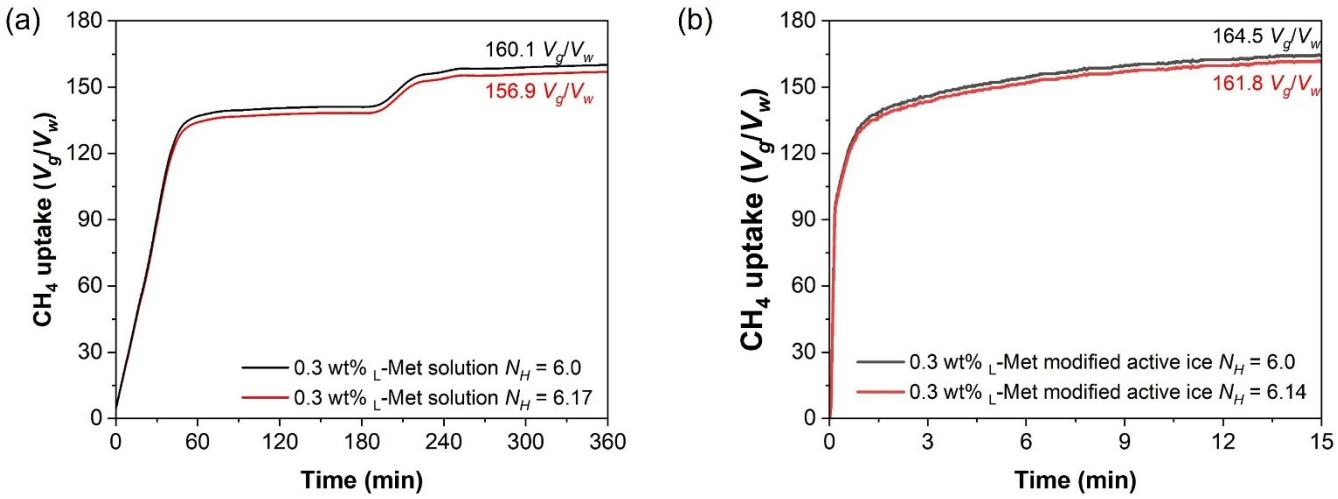

Fig. S14. Sensitivity Analysis of hydration number for CH_4 uptake: (a) 0.3 wt% $_L$-Met solution; and (b) 0.3 wt% $_L$-Met solution.

It is also worth noting that the fixed hydration number of 6.0 is the standard theoretical value widely adopted for CH_4 sI hydrates. Using this value facilitates direct comparison with the majority of reported results in the existing literature. Therefore, adopting N_h = 6.0 provides a reasonable and consistent basis for calculating methane uptake in this study.

Table S4. Calculated hydration number (N_H) and cage occupancy (θ_L *and* θ_S) of CH_4 hydrate formed in $_L$-Met solution and $_L$-Met modified active ice systems.

System	Concentration (wt%)	Run	I_L (a.u.)	I_S (a.u.)	θ_L (%)	θ_S (%)	N_H
Solution	0.03	Run 1	4104.5	115.6	97.86	80.25	6.15
		Run 2	4785.9	1367.4	97.72	83.76	6.10
		Average	——	——	97.79 ± 0.09	82.01 ± 2.48	6.12 ± 0.04
	0.3	Run 1	1106.7	410.1	99.82	89.79	6.22
		Run 2	1175.09	425.4	99.66	91.76	6.13
		Average	——	——	99.74 ± 0.11	90.77 ± 1.39	6.17 ± 0.06
	3.0	Run 1	11593.1	11827.1	97.42	86.08	6.06
		Run 2	3414.3	3912.2	96.24	95.50	5.98
		Average	——	——	96.83 ± 0.83	90.79 ± 6.66	6.02 ± 0.05
Active ice	0.03	Run 1	7461.5	2495.1	96.19	96.51	5.97
		Run 2	9843.8	3118.9	97.08	92.27	5.99
		Average	——	——	96.63 ± 0.63	94.39 ± 2.99	5.98 ± 0.01
	0.3	Run 1	8242.5	7158.1	99.28	93.54	6.05
		Run 2	2918.3	2328.8	96.74	94.42	5.97

		Average	——	——	98.01 ± 1.79	93.98 ± 0.62	6.01 ± 0.05
	3.0	Run 1	2708.3	796.9	98.7	86.15	6.07
		Run 2	1900.8	704.3	99.82	89.81	6.22
		Average	——	——	98.71 ± 0.02	87.98 ± 2.59	6.14 ± 0.11

1.11. Schematic of the Raman probe position during CH_4 hydrate formation from 0.3 wt% $_L$-Met modified active ice

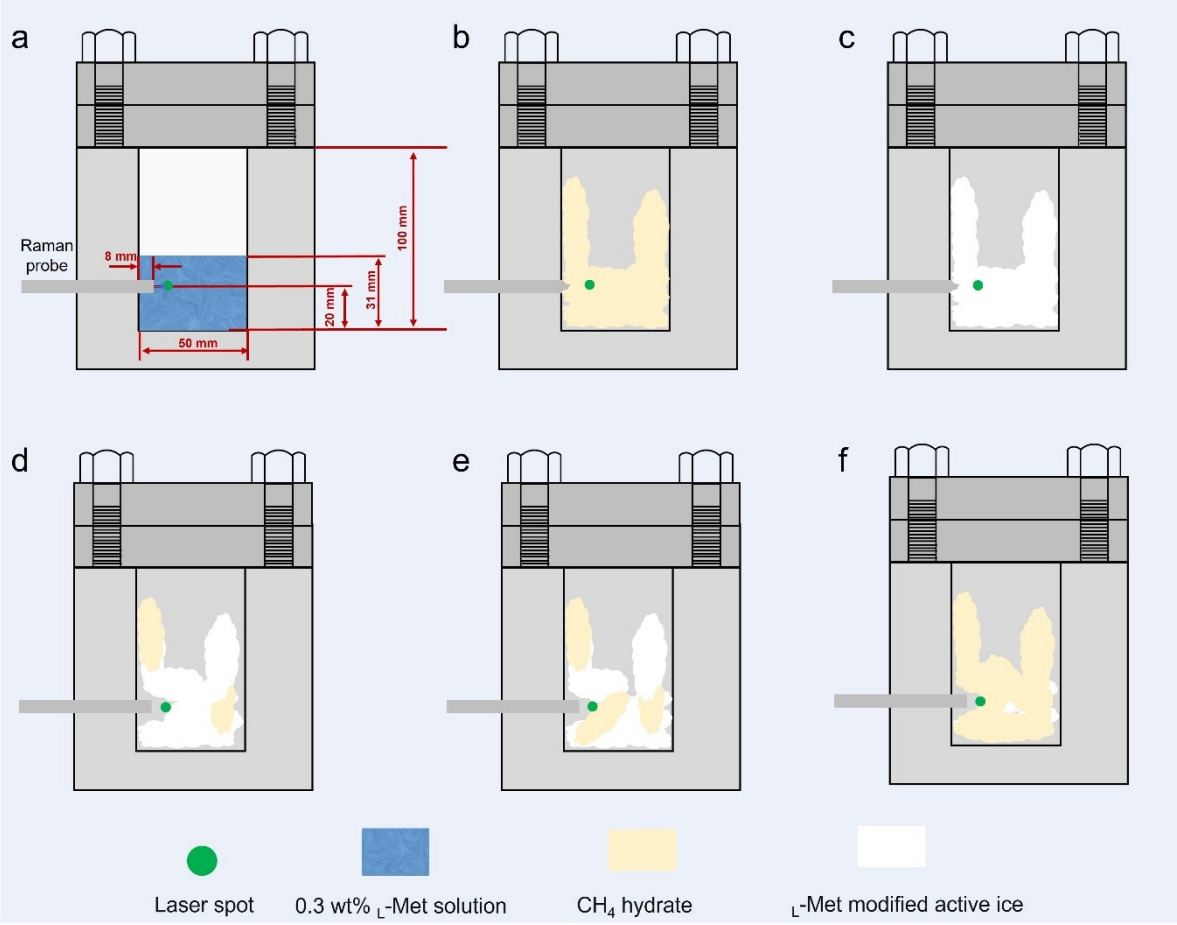

Fig. S15. Schematic diagram of the information measured by the Raman probe during the synthesis of 0.3 wt% $_L$-Met modified active ice and its application to form CH_4 hydrate.

Fig. S15 illustrates the schematic of the Raman probe monitoring the entire process of CH_4 hydrate formation from 0.3 wt% $_L$-Met solution (stage I), dissociation to form $_L$-Met modified active ice (stage II), and formation from the 0.3 wt% $_L$-Met modified active ice (stage III). At stage I, the Raman probe was inserted into the liquid phase (0.3 wt% $_L$-Met solution). As CH_4 hydrate began to form, the Raman probe was wholly and gradually encapsulated by newly formed CH_4 hydrate. During the subsequent depressurization stage, the dissociated water did not liquefy but rapidly refroze to form $_L$-Met modified active ice, which almost entirely preserved the original morphology of the CH_4 hydrate.[5]

Upon reinjection of CH_4 gas (stage III), the rising gas temperature caused rapid melting of the surface $_L$-Met modified active ice, and CH_4 hydrate nucleated on the ice surface, as evidenced by the rapid pressure

drop. However, the active ice near the Raman probe only partially melted and had not yet transformed into CH_4 hydrate; therefore, the Raman signal initially detected a distinct gas-phase CH_4 peak. As melting progressed, more CH_4 gas accumulated near the probe, and the intensity of the gas-phase peak gradually increased (see Fig. 4i). At 2.5 min, the active ice within the laser spot area transformed into CH_4 hydrate, resulting in the appearance of the characteristic peak at 2905.2 cm^{-1}, corresponding to CH_4 molecules occupying the $5^{12}6^2$ large cages of the sI hydrate. Subsequently, as the laser spot likely illuminated both the porous hydrate and adjacent gas regions, coexistence of gaseous CH_4 and CH_4 hydrate was still observed in the Raman spectra.

Section 2. Methodological details and validation of CH_4 uptake calculation

2.1 Temperature and pressure evolution during CH_4 hydrate formation from 0.3 wt% $_L$-Met modified active ice

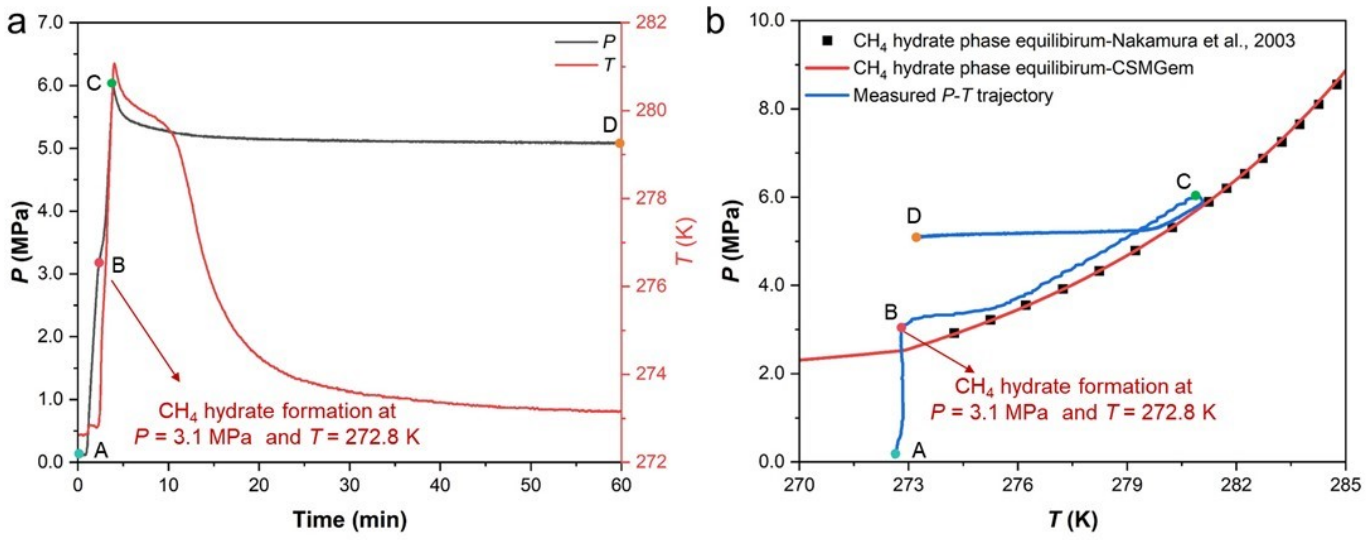

Fig. S16. (a) Temperature-pressure (*T*-*P*) evolution during CH_4 hydrate formation from 0.3 wt% $_L$-Met modified active ice at $T = 272.7$ K and $P = 6.0$ MPa; (b) measured *T*-*P* trajectory in relation to the CH_4 hydrate phase equilibrium curve.[6]

Fig. S16(a) shows the real-time pressure and temperature profiles during CH_4 hydrate formation from 0.3 wt% $_L$-Met modified active ice. CH_4 hydrate began to form at around $P = 3.1$ MPa and $T = 272.8$ K during the CH_4 injection process, leading to a slowdown in the pressure rise and a noticeable increase in temperature, as shown in Fig. S16 (b). When the CH_4 gas injection was completed, the pressure decreased rapidly, indicating the rapid formation of CH_4 hydrate.

2.2 Effect of ideal and real gas assumptions on compressibility factor and CH_4 uptake

To illustrate this effect quantitatively, we performed a comparative analysis using the representative case of CH_4 hydrate formation in the optimized 0.3 wt% $_L$-Met modified active ice system. Under the reacting *P*-*T* conditions, the real-gas compressibility factor $Z(t)$, calculated via PR-EOS, deviates significantly from unity, ranging between 0.78 and 0.92. The ideal gas assumption fixes $Z = 1$ (see Fig. S2).

This deviation has a profound impact on the calculated CH_4 uptake. The final CH_4 uptake calculated

using the PR-EOS correction is 150.68 V_g/V_w, whereas the ideal-gas assumption yields only 95.07 V_g/V_w. Neglecting real-gas behavior would therefore result in a substantial underestimation of storage capacity by approximately 37%. The effect on t_{90} is less pronounced but still measurable. The t_{90} calculated with PR-EOS is 2.84 min, compared to 3.09 min under the ideal assumption, representing an 8.8% difference.

The discrepancy in CH_4 uptake is directly proportional to the *Z*-factor error. However, t_{90} is a kinetic parameter defined based on the relative percentage of reaction completion (i.e., time to reach 90% of the final CH_4 uptake). Although the absolute final capacity changes significantly, the overall shape and trend of the reaction curve remain similar. Therefore, the relative time scale reflected by t_{90} is less sensitive to the *Z*-factor correction than the absolute storage value. In conclusion, this quantification confirms that employing the PR-EOS to correct for gas compressibility is indispensable for ensuring the accuracy of our reported data.

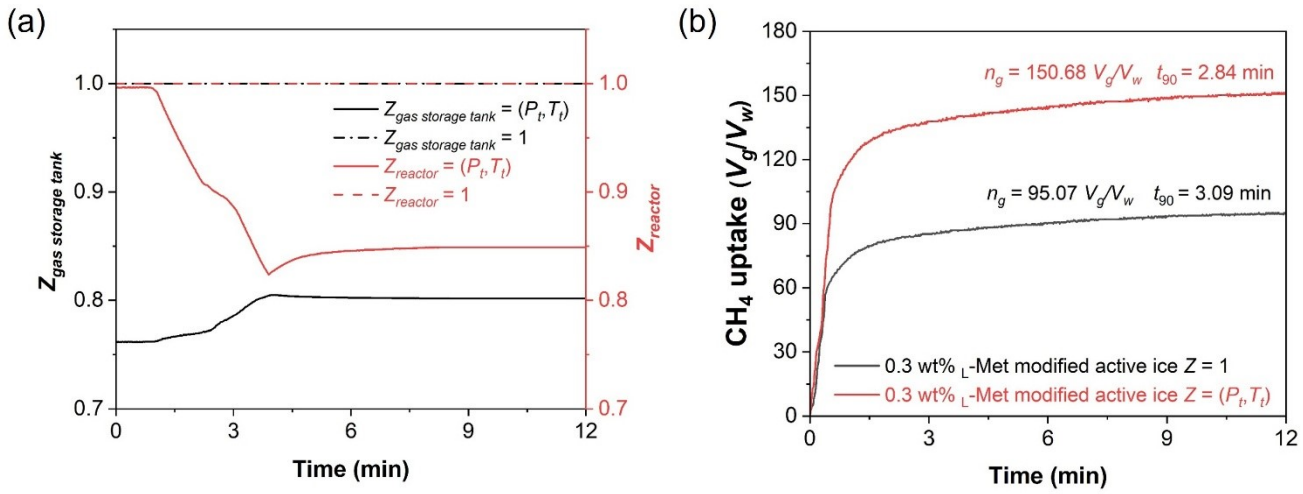

Fig. S17. Validation of compressibility factors (*Z*) calculated by PR-EOS (solid lines) versus the ideal gas assumption (Z = 1, dashed lines); (b) comparison of CH_4 uptake profiles calculated based on *Z* derived from (*P*, *T*) and *Z* = 1.

1.3 Verification of calculation methodology during CH_4 hydrate formation from $_L$-Met modified active ice

After the CH_4 hydrate formation from 0.3 wt% $_L$-Met modified ice, the system was subjected to slow heating to dissociation. This slow process avoids transient temperature and pressure gradients, allowing for an accurate thermodynamic calculation of the total CH_4 actually stored. We compared the amount calculated

during the ultra-rapid formation process (using our molar and volume balance method) with the amount measured during the slow dissociation. process. The calculated CH_4 uptake was 0.112 mol, while the measured CH_4 release was 0.110 mol, corresponding to a negligible difference of only 1.8% (see Fig. S18). Although absolute values vary slightly from the main manuscript due to different reactor specifications used for validation, the gas-to-liquid ratio remained consistent. This excellent agreement provides robust independent validation of our methodology's accuracy. Furthermore, the long-term pressure stability observed at the end of both the formation and dissociation stages confirmed that the system maintained a constant pressure over time, proving there was no CH_4 gas leakage to the external environment.

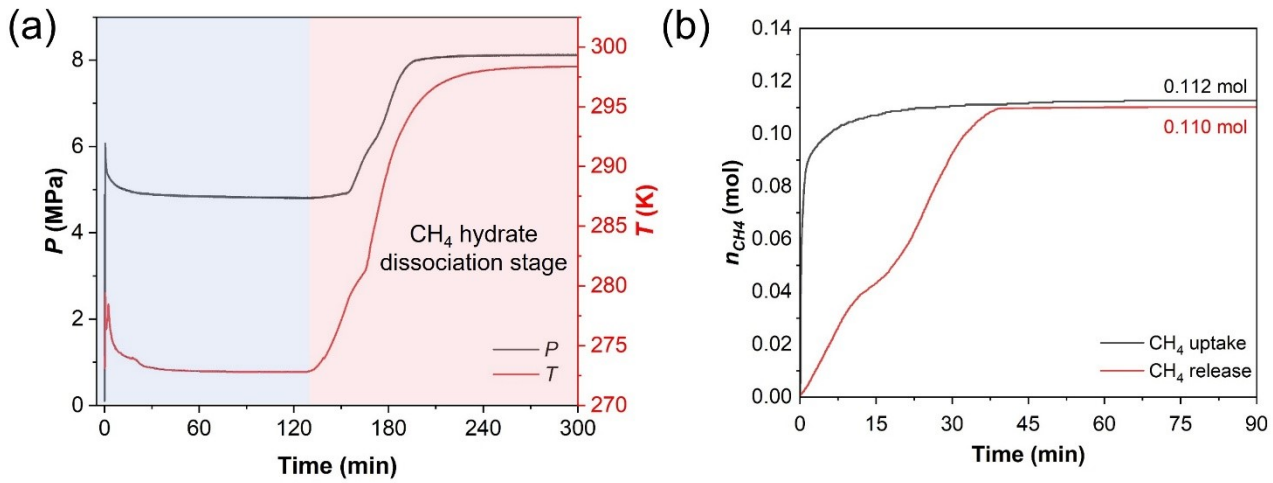

Fig. S18. (a) Pressure and temperature profiles over time during the CH_4 hydrate formation and dissociation from 0.3 wt% $_L$-Met; (b) Molar quantity of CH_4 involved in hydrate formation and subsequent dissociation.

1.4 Distribution of CH_4 among the gas phase, dissolved phase, and hydrate phase

For the $_L$-Met solution system, we calculated the solubility using Henry's Law, the methodology detailed in our previous work. The results indicate that at the end of CH_4 hydrate formation (t = 420 min), the dissolved CH_4 accounts for only 0.1% of the total CH_4, whereas the CH_4 gas phase and CH_4 hydrate phase account for 45.3% and 54.6%, respectively (see Fig. S19). Given this negligible proportion, our discussion primarily focuses on the CH_4 storage capacity within the hydrate phase.

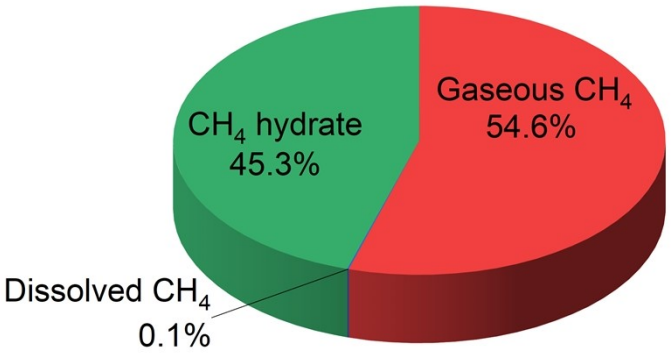

Fig. S19. Distribution of CH_4 among the gas phase, dissolved phase, and hydrate phase for the 0.3 wt% $_L$-Met solution system at t = 420 min.

Section 3 Macroscopic kinetic results of CH_4 hydrate formation from $_L$-Methionine solution and active ice

3.1 Pressure, temperature, and morphology evolution of CH_4 hydrate formation

To substantiate the proposed self-sustaining melting-formation feedback loop, we performed a comparative analysis of the real-time pressure, temperature, and morphology evolution between the $_L$-Met solution and the $_L$-Met modified active ice. As shown in Fig. S20, the process includes CH_4 gas injection (stage A-B) followed by CH_4 hydrate formation (stage B-F). Although the external water bath was kept constant, distinct temperature excursions were observed multiple times during Stage B-F (indicated by the red curve). Since there is no internal heat sink, the substantial heat released from rapid CH_4 hydrate formation accumulates, converting into sensible heat that raises the reactor temperature.

In contrast, for $_L$-Met modified active ice system, after CH_4 gas injection (stage C-E), the pressure drops rapidly and continuously, indicating massive and rapid CH_4 hydrate formation, but no significant temperature increase was observed during this intense formation period. The temperature profile remained remarkably stable. The absence of a temperature spike, despite the generation of large amounts of reaction heat, provides compelling evidence that the heat was instantaneously consumed. In this system, a significant portion of the heat released during CH_4 hydrate formation is likely dissipated through absorption by the surrounding ice. This striking contrast serves as a robust experimental verification of the proposed feedback loop. The heat

released by CH_4 hydrate formation is efficiently balanced by the melting of the surrounding ice, which in turn creates liquid pockets that further accelerate the reaction.

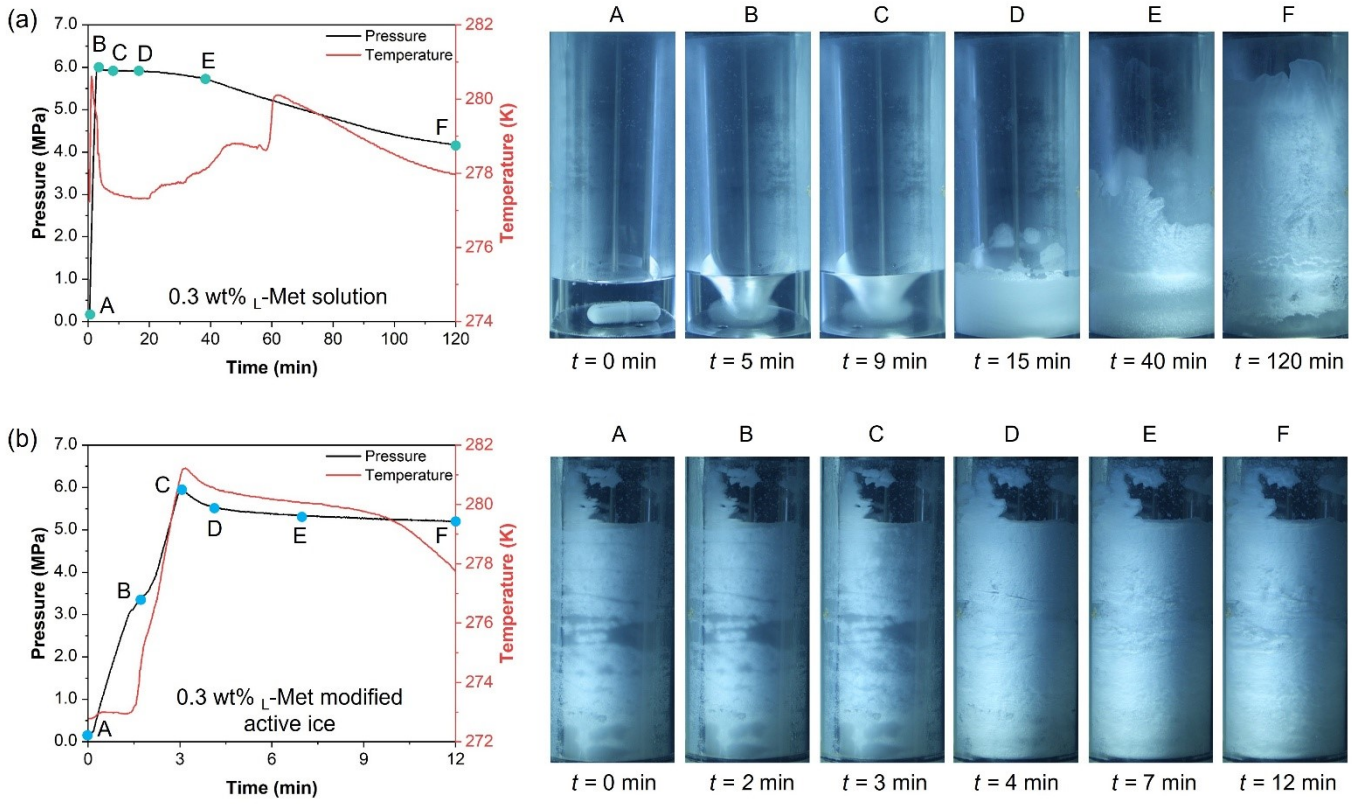

Fig. S20. Pressure, temperature, and morphology evolution of CH_4 hydrate formation from (a) 0.3 wt% $_L$-Met solution and (b) 0.3 wt% $_L$-Met modified active ice.

3.2 Comparison of CH_4 hydrate formation kinetics from $_L$-Met solution and from $_L$-Met modified active ice

Table S5. Summary of the initial phase, temperature (T), initial pressure (P), the time required for 90% completion of the final CH_4 uptake (t_{90}), final CH_4 uptake, the conversion of water to CH_4 hydrate (C_w), and $I_{DDAA/DA}$ for all the investigated systems.

$C_{L\text{-}Met}$ (wt%)	Initial phase	T (K)	P (MPa)	t_{90} (min)	Final CH_4 uptake (V_g/V_w)	C_w (%)	$I_{DDAA/DA}$
0	Pure water	from 277.2 to 272.7	6.0	211.17 ± 25.69	30.12 ± 1.74	13.94 ± 0.81	0.89 ± 0.04
	Pure ice	272.7		0.99 ± 0.57	12.29 ± 5.03	5.69 ± 2.33	1.35 ± 0.05
0.03	$_L$-Met solution	from 277.2 to 272.7		206.14 ± 0.19	154.54 ± 3.52	71.54 ± 1.63	0.82 ± 0.01
	$_L$-Met modified active ice	272.7		10.54 ± 1.53	116.16 ± 4.34	53.78 ± 2.01	1.25 ± 0.02
0.3	$_L$-Met solution	from 277.2 to 272.7		242.84 ± 0.47	154.48 ± 3.63	71.52 ± 1.68	0.81 ± 0.01
	$_L$-Met modified active ice	272.7		3.33 ± 0.43	156.05 ± 3.28	72.24 ± 1.52	1.05 ± 0.08
3.0	$_L$-Met solution	from 277.2 to 272.7		234.45 ± 1.34	150.78 ± 4.58	69.81 ± 2.12	0.83 ± 0.02
	$_L$-Met modified active ice	272.7		4.56 ± 0.95	136.83 ± 6.72	63.35 ± 3.11	0.83 ± 0.01

3.3 Effect of CH_4 diffusion and reactor scale-up on CH_4 hydrate formation from $_L$-Met modified active ice

It should be note that the CH_4 diffusion behavior in the $_L$-Met modified active ice system may be fundamentally different from that in a traditional dense pure ice system due to the distinct microstructure of the active ice. Cryo-SEM characterization demonstrates that the 0.3 wt% $_L$-Met modified active ice exhibits a loose and highly porous structure, with pore sizes in the range of 7-17 μm, whereas pure ice presents a dense structure. This structural difference leads to a diffusion mechanism that deviates significantly from the conventional case.

To illustrate this distinction more clearly, two shrinking-core schematic models have been added in Fig. S21: (a) the conventional shrinking-core model for pure ice and (b) the proposed shrinking-core model for porous $_L$-Met modified active ice. In the traditional dense pure ice system, CH_4 hydrate formation is essentially a surface-controlled reaction. As hydrate nucleates and grows, CH_4 is rapidly consumed at the ice-gas interface, leading to a sharp depletion of CH_4 concentration near the surface. Once a dense CH_4 hydrate shell forms, it acts as a physical barrier that severely limits further CH_4 diffusion into the interior, resulting in a diminishing concentration gradient and suppressed CH_4 hydrate growth.

In contrast, the $_L$-Met modified active ice possesses an interconnected porous framework that allows CH_4 to readily diffuse into the interior of the ice matrix. As a result, the CH_4 concentration within the active ice remains nearly uniform throughout the reaction, maintaining a sustained driving force for CH_4 hydrate formation across the entire core. Even as the reaction proceeds, the hydrate phase formed remains relatively porous, enabling CH_4 molecules to bypass solid-state diffusion limitations. Consequently, CH_4 diffusion plays only a minor role in the late-stage kinetic deceleration.

Furthermore, to address the reactor scale effects, we conducted additional validation experiments using reactors with different internal volumes (125.0 mL, 256.4 mL, and 626.8 mL), as illustrated in Fig. S22 (a)-(c). These reactors differ significantly in characteristic length scales and gas-solid contact area, thereby

allowing an explicit assessment of possible scale-dependent effects on CH_4 hydrate formation kinetics. To ensure the comparability of the experiments, the same gas-liquid molar ratio was maintained for all reactor configurations. Specifically, 15 mL, 40 mL, and 95 mL of 0.3 wt% $_L$-Met solution were added to the 125.0 mL, 256.4 mL, and 626.8 mL reactors, respectively, to form $_L$-Met modified active ice. All kinetic experiments were carried out at an initial pressure of 6 MPa and a temperature of 272.7 K.

As shown in Fig. S22 (d) and (e), the kinetic performance remains remarkably consistent across the different scales. Specifically, the final CH_4 uptake exhibited only a minor variation of approximately 9.5%, decreasing slightly from 164.5 V_g/V_w to 148.8 V_g/V_w as the reactor volume increased five-fold. Notably, the growth rate even shows a faster tendency with increasing reactor size, as evidenced by the time required to reach 90% of the final CH_4 uptake (t_{90}) actually decreased from 4.60 min in the 125.0 mL reactor to 2.52 min in the 626.8 mL reactor. Meanwhile, the normalized formation rate at 90% uptake (NRt_{90}) increased significantly from 35.76 V_g/V_w/min to 59.05 V_g/V_w/min.

This sustained kinetic efficiency suggests that the evolving CH_4 hydrate layer does not impose a significant diffusion barrier. While CH_4 diffusion through hydrate layers can be a rate-limiting factor in pure ice systems, the $_L$-Met modified active ice in this study promotes the formation of a loose and porous hydrate structure, which is directly confirmed by cryo-SEM observations. This high porosity ensures that the CH_4 hydrate layer remains highly permeable to CH_4 gas, allowing CH_4 molecules to penetrate through micro-scale channels to reach the reaction interface. Consequently, the mass transfer resistance remains low despite the increase in CH_4 hydrate layer thickness or changes in reactor scale.

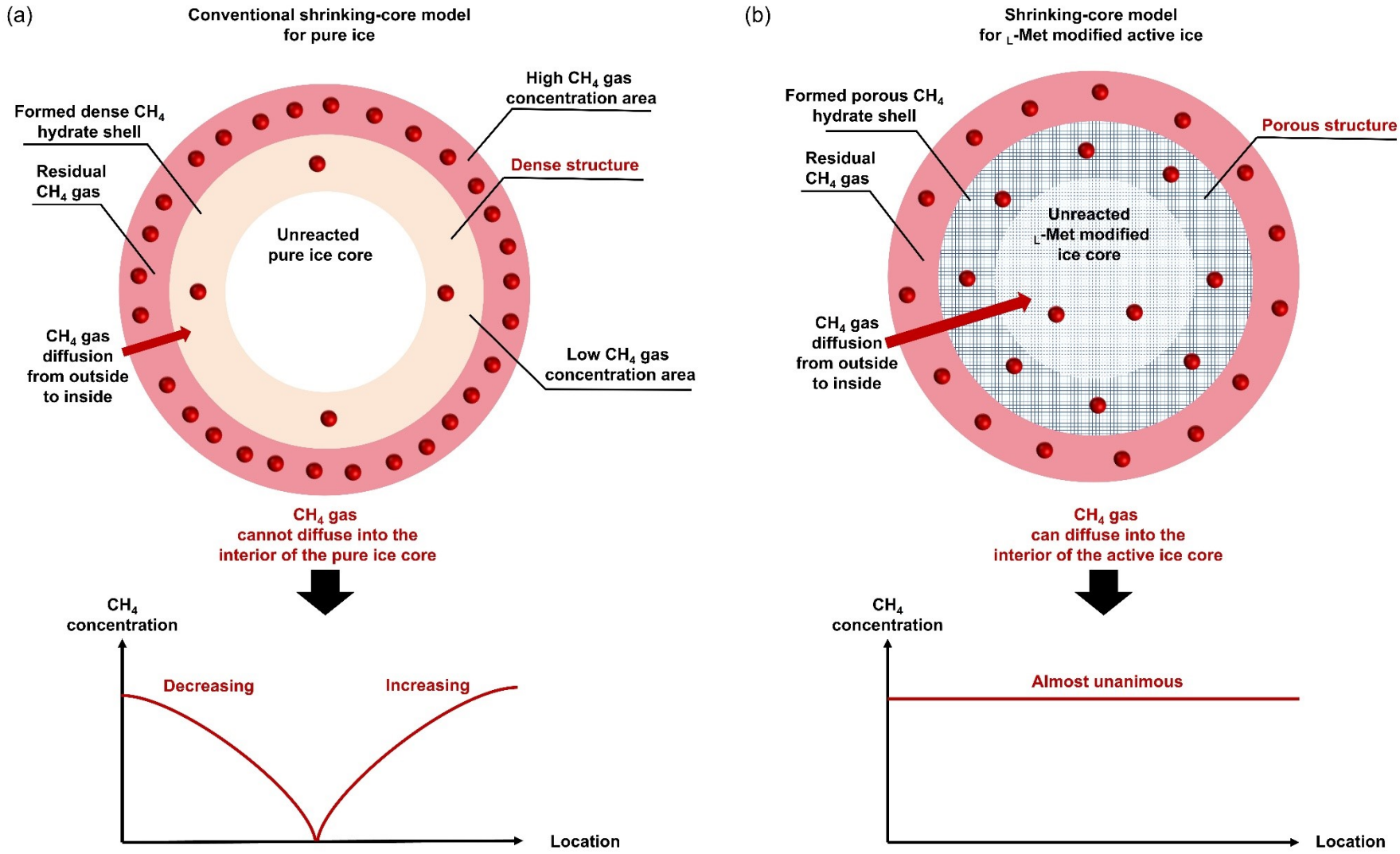

Fig. S21. Schematic of the (a) conventional shrinking-core model for pure ice; (b) proposed shrinking-core model for $_L$-Met modified active ice

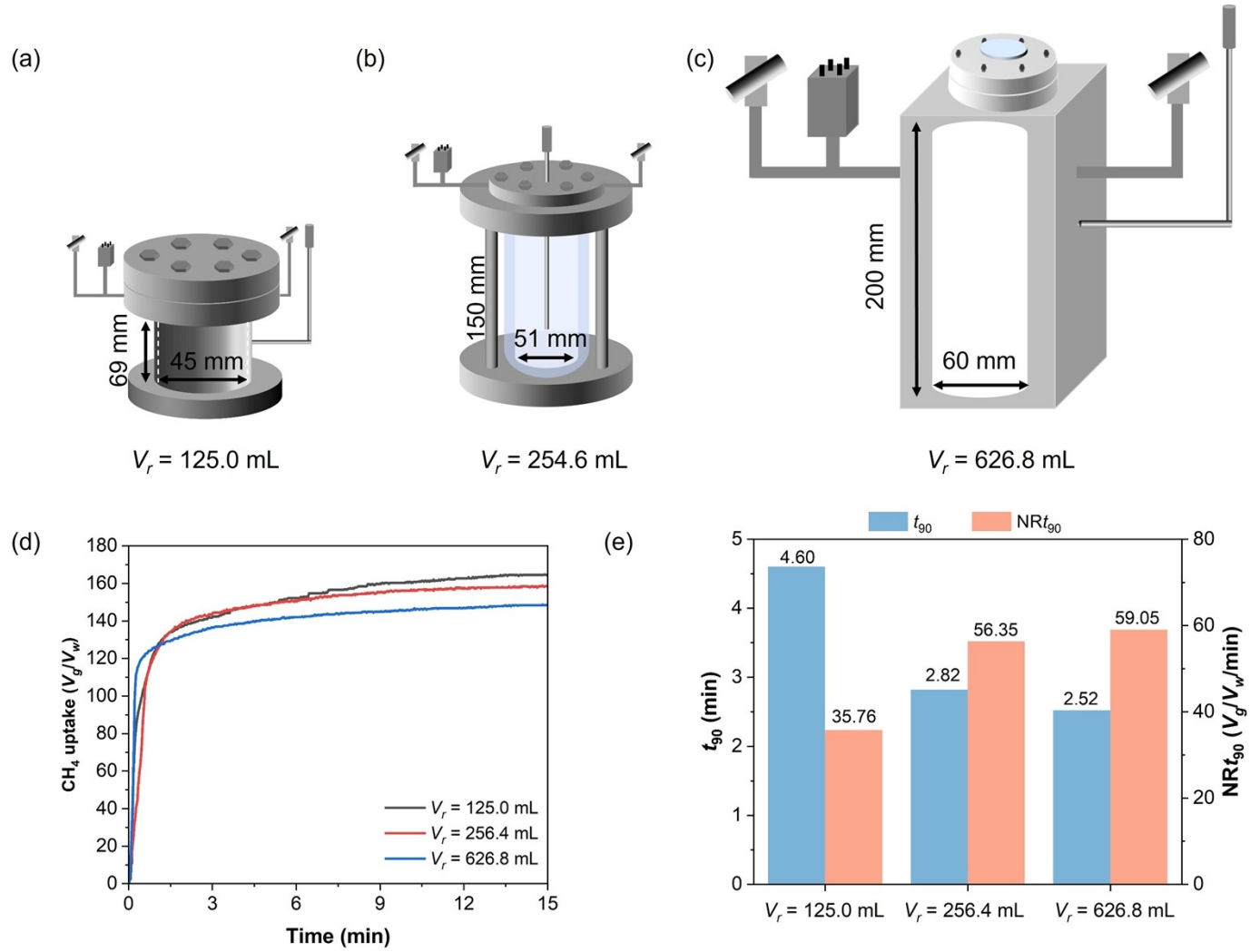

Fig. S22. Schematic diagrams of the three reactors used in this study: (a) cylindrical reactor with an internal volume (V_r) of 125.0 mL; (b) cylindrical reactor with V_r of 254.6 mL; and (c) cuboid reactor with V_r of 626.8 mL; assessment of reactor scale and geometry effects on CH_4 hydrate formation from 0.3 wt% $_L$-Met modified active ice at P = 6.0 MPa and T =272. 7 K: (d) time-dependent CH_4 uptake profiles across the three scales; (e) comparison of kinetic final CH_4 uptake and the time required to reach 90% of the final uptake (t_{90}).

We sincerely thank the reviewer for the valuable suggestions, which have provided new insights and clear directions for our future research. In subsequent studies, we will design and conduct systematic experiments to quantitatively determine key mass transfer parameters in the $_L$-Met modified active ice system, including the effective CH_4 mass transfer coefficient, the amount of CH_4 converted into CH_4 hydrate within the porous ice matrix, as well as the local CH_4 gas concentration gradients. In addition, the effects of reactor size and gas-liquid contact area on CH_4 gas transport and CH_4 hydrate formation behavior will be

systematically evaluated. Based on these quantitative data, a more comprehensive kinetic model will be established, explicitly coupling heat and mass transfer limitations with intrinsic reaction kinetics. This will enable a deeper and more quantitative understanding of the interplay between heat/mass transfer, reactor-scale effects, and intrinsic reaction kinetics during CH_4 hydrate formation from $_L$-Met modified active ice.

3.4 Effects of $_L$-Met concentrations on the morphology evolution of CH_4 hydrate

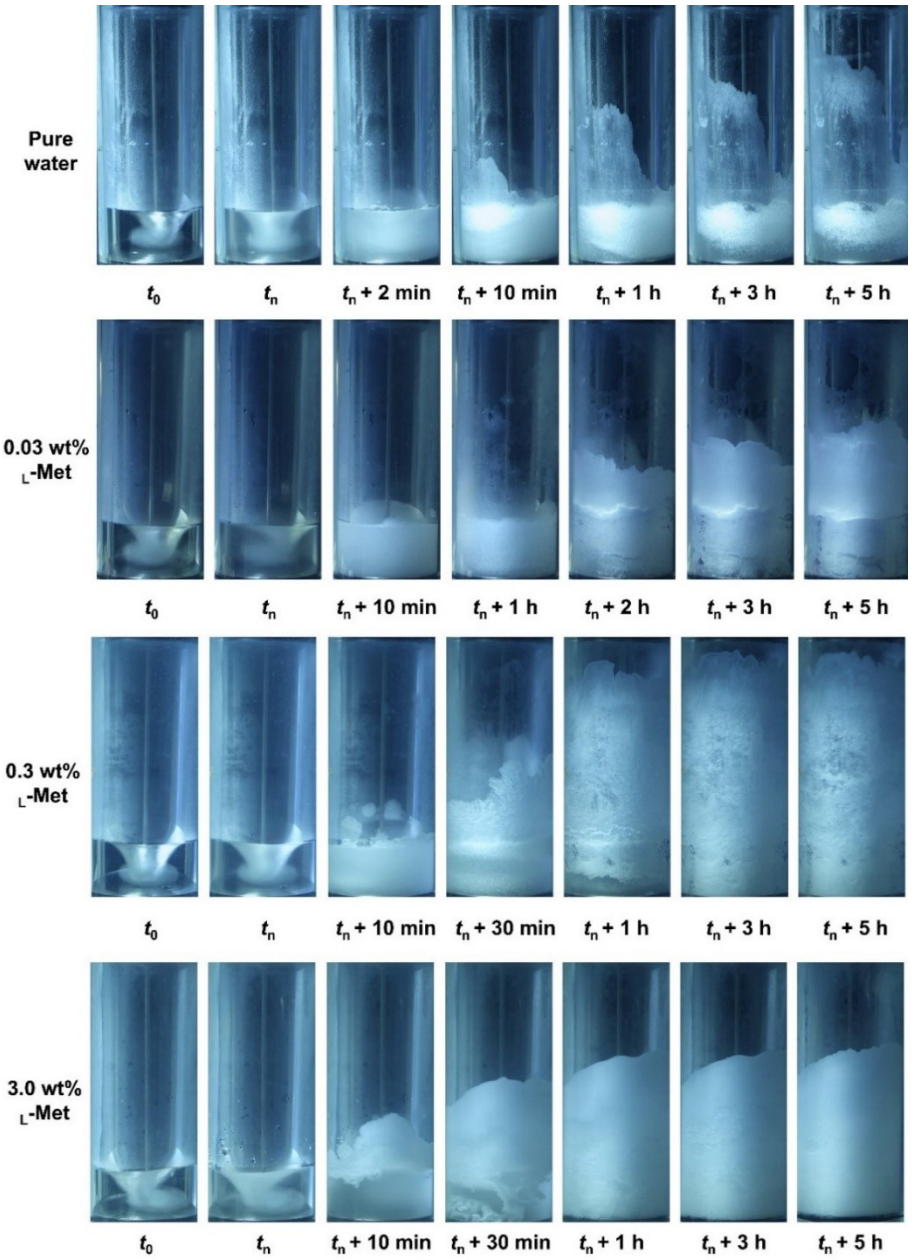

Fig. S23. Morphological evolution of CH_4 hydrate formation from the different concentrations (0–3.0 wt%) of $_L$-Methionine at an initial pressure of 6.0 MPa, with temperature maintained at 277.2 K for 3 h and subsequently decreased to 272.7 K.

Fig. S23 presents the morphology evolution of CH_4 hydrate growth in pure water and $_L$-Met solutions

with concentrations of 0.03 wt%, 0.3 wt%, and 3.0 wt%. In all cases, CH_4 hydrate nucleation initiated in the liquid phase and subsequently propagated toward the gas phase, suggesting that $_L$-Met primarily modifies the interfacial characteristics and internal structure of the forming CH_4 hydrate layer rather than altering the nucleation pathway. In the pure water system, once CH_4 hydrate nucleated, a thin and compact hydrate film rapidly developed at the gas–liquid interface, which severely impedes further contact between CH_4 and water, thus limiting hydrate growth.[7] When a low concentration of $_L$-Met (0.03 wt%) is introduced, the CH_4 hydrate growth displays a distinct stratified morphology. In contrast, at 0.3 wt% $_L$-Met, the CH_4 hydrate exhibited a loose, porous structure that extends throughout almost the entire reactor volume, implying enhanced gas diffusion. However, when the $_L$-Met concentration increases to 3.0 wt%, the overall hydrate height decreases, and the deposits appear denser and more compact.

3.5 Effects of $_L$-Met concentrations on the morphology evolution during CH_4 hydrate dissociation and forming active ice

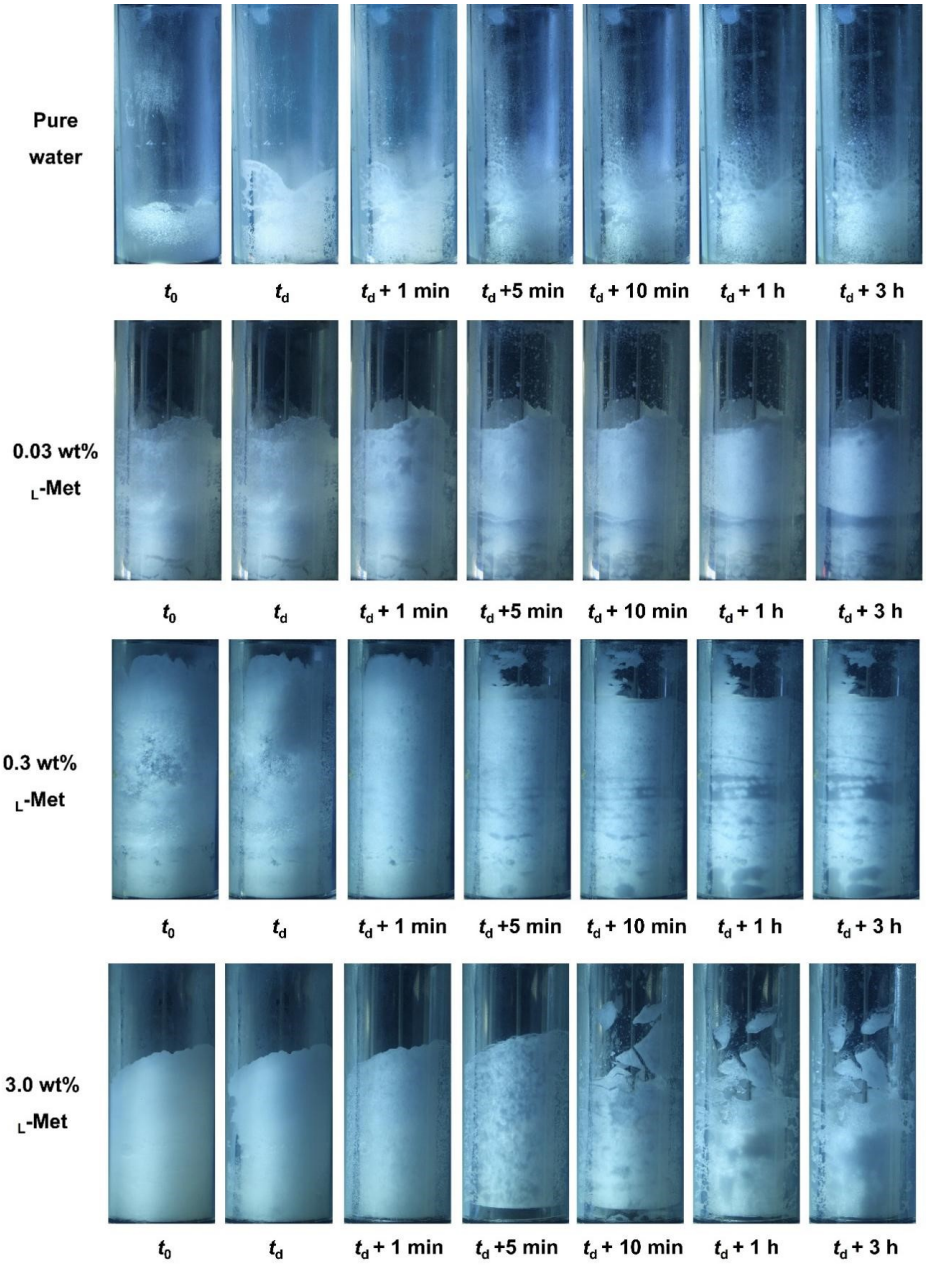

Fig. S24. Morphological evolution of CH_4 hydrate dissociation to form $_L$-Met modified active ice containing different concentrations (0–3.0 wt%) of $_L$-Met at P = 0.1 MPa and T = 272.7 K.

Fig. S24 presents the morphological evolution during the formation of $_L$-Met modified active ice from the dissociation of preformed CH_4 hydrates in different concentrations of $_L$-Met solutions. The results show that in pure water, 0.03 wt% and 0.3 wt% $_L$-Met systems, the active ice largely retains the structural features of the initial CH4 hydrate, exhibiting a relatively stable morphology without significant structural disruption.

In contrast, at 3.0 wt% $_{L}$-Met, the initial CH_4 hydrate structure of active ice became increasingly unstable over time, showing progressive fracturing. This observation suggests that an excessive $_{L}$-Met concentration has a destructive effect on the integrity of the initial CH_4 hydrate structure.

3.6 Effects of $_{L}$-Met on the morphology evolution of CH_4 hydrate formation from active ice

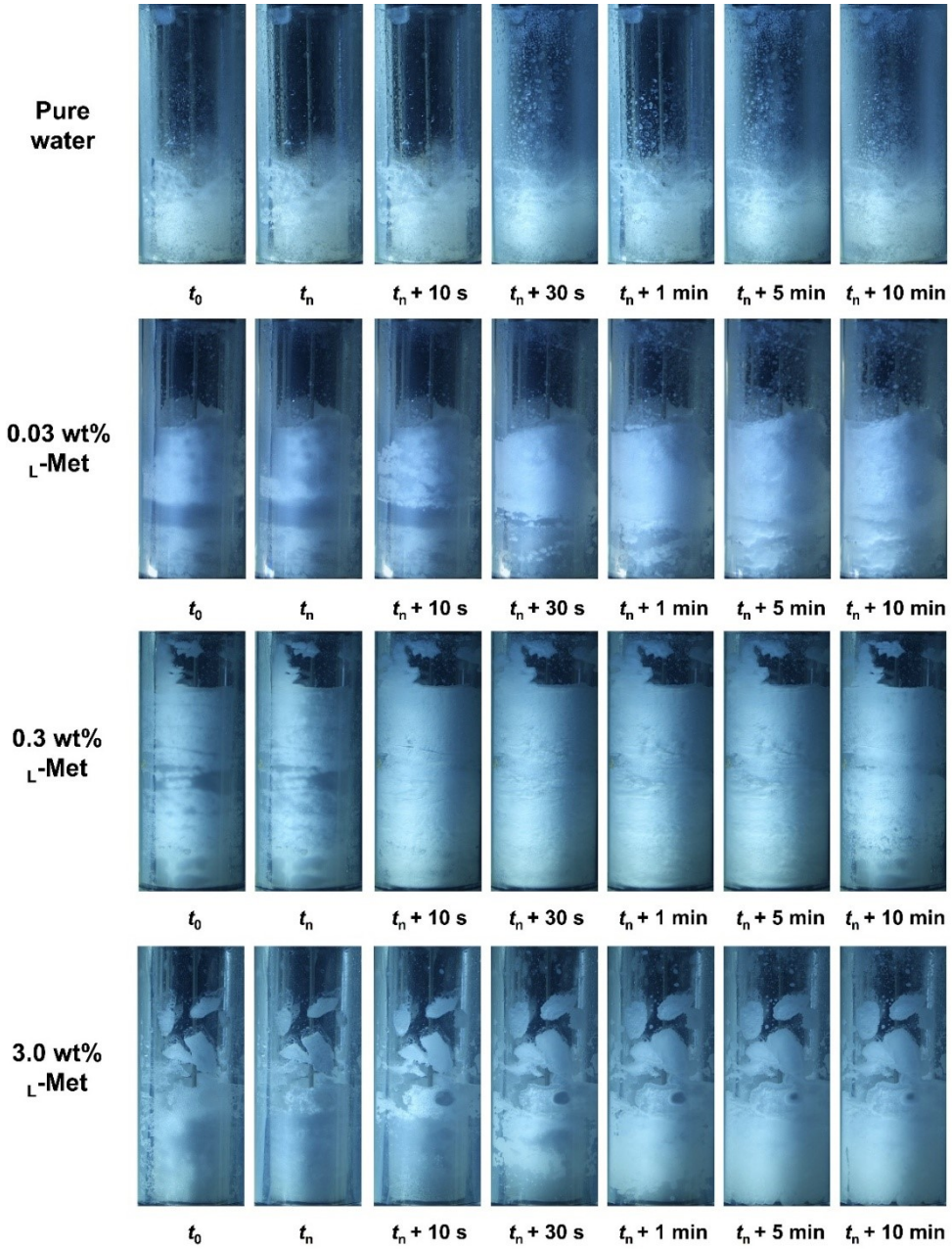

Fig. 25. Morphological evolution of CH_4 hydrate formation from the $_{L}$-Met modified active ice containing different concentrations (0–3.0 wt%) of $_{L}$-Met at P = 6.0 MPa and T = 272.7 K.

Fig. S25 illustrates the morphological evolution of CH_4 hydrate formation from pure ice (blank control) and $_{L}$-Met modified active ice with different concentrations (0.03 wt%, 0.3 wt%, and 3.0 wt%). In the pure

ice system, only a small amount of CH_4 hydrate is formed, with no significant change in overall morphology. In contrast, all $_L$-Met modified active ice systems exhibit a similar hydrate growth pattern, where CH_4 hydrate nucleates on the ice surface and subsequently propagates into the ice interior. Throughout this process, a clear synergy between ice melting and hydrate formation was observed, while CH_4 hydrate growth remained confined within the ice layer without noticeable outward expansion. Specifically, the 0.03 wt% $_L$-Met modified active ice exhibited relatively slow ice melting and hydrate growth. In contrast, the 0.3 wt% system, where the ice layer entirely covers the reactor and maintains efficient contact with the gas phase, showed the fastest rates of both melting and CH_4 hydrate formation. In contrast, the 3.0 wt% $_L$-Met system displays slower kinetics due to the structural incompleteness of the ice layer.

3.7 Chemical and physical contributions of $_L$-Met modified active ice to CH_4 hydrate formation

To rigorously disentangle the chemical promotion effects of $_L$-Met from the physical effects of the active ice structure, we have performed a series of additional control experiments. The results are summarized below.

(1) 0.3 wt% hydrophilic $_L$-Arg modified active ice vs. 0.3 wt% hydrophobic $_L$-Met modified active ice: Fig. S26(a) presents a comparison of the chemical structures and key physicochemical properties of $_L$-Met and $_L$-Arg. The hydropathy index indices highlight the hydrophobic nature of $_L$-Met (+1.9) and the strong hydrophilic of $_L$-Arg (-4.5). To isolate the effect of hydrophobic modification, active ice was synthesized with 0.3 wt% $_L$-Arg (hydrophobic) and compared with $_L$-Met (hydrophilic) under identical experimental conditions (P = 6 MPa, T = 272.7 K) for CH_4 hydrate formation (see Fig. S26(b)). The results show that the CH_4 uptake for 0.3 wt% $_L$-Arg modified active ice was extremely low (21.9 V_g/V_w), representing an 86.7% decrease compared to the 0.3 wt% $_L$-Met modified active ice (164.5 V_g/V_w). Although the $_L$-Arg modified active ice growth rate reached faster, its CH_4 storage capacity remained negligible and too low for practical applications. This indicates that the physical structure of active ice alone, without hydrophobic surface modification, is insufficient for effective high-capacity hydrate storage.

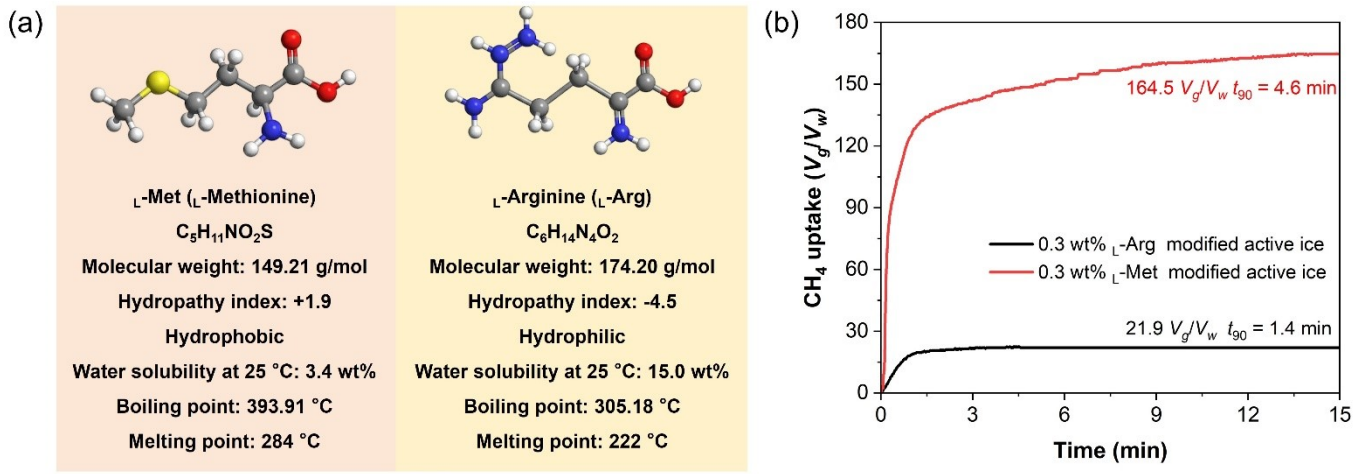

Fig. S26(a) Comparison of physicochemical properties of $_{L}$-Methionine ($_{L}$-Met) and $_{L}$-Arginine ($_{L}$-Arg); Comparison of the CH_4 hydrate formation kinetics for 0.3 wt% $_{L}$-Arg modified active ice and 0.3 wt% $_{L}$-Met modified active ice at P = 6 MPa and T = 272.7 K.

(2) 0.3 wt% $_{L}$-Met solution vs. 0.3 wt% $_{L}$-Met modified active ice: Under the same experimental conditions (P = 6 MPa, T = 272.7 K, and 0.3 wt% $_{L}$-Met), the CH_4 hydrate formation kinetics in the $_{L}$-Met solution system were added as a control. Unlike the $_{L}$-Met modified active ice system, the $_{L}$-Met solution system required mechanical stirring (400 rpm) to induce nucleation. As shown in Fig. S27, the CH_4 uptake for the 0.3 wt% $_{L}$-Met solution system was 142.3 V_g/V_w, which is approximately 13.5% lower than that of the 0.3 wt% $_{L}$-Met modified active ice system (164.5 V_g/V_w). Furthermore, the t_{90} significantly extended to 26.3 min, compared to just 4.6 min for the active ice system. This indicates that the chemical presence of $_{L}$-Met alone, without the physical effects of active ice, results in significantly slower kinetics and lower capacity.

This also explains why the initial CH_4 hydrate formation (stage I) in this study was conducted in two steps. In the 1st step, the system was stabilized at 277.2 K for 3 hours, followed by 2nd step in which the temperature was lowered to 272.7 K (see Fig. 2a). This process led to the formation of a greater amount of CH_4 hydrate, resulting in an increased CH_4 uptake of 154.48 V_g/V_w, compared with the direct injection of CH_4 gas at 272.7 K and 6.0 MPa (142.3 V_g/V_w). Upon dissociation to $_{L}$-Met modified active ice, it generated more $_{L}$-Met modified active ice that further promoted CH_4 hydrate formation in the stage III.

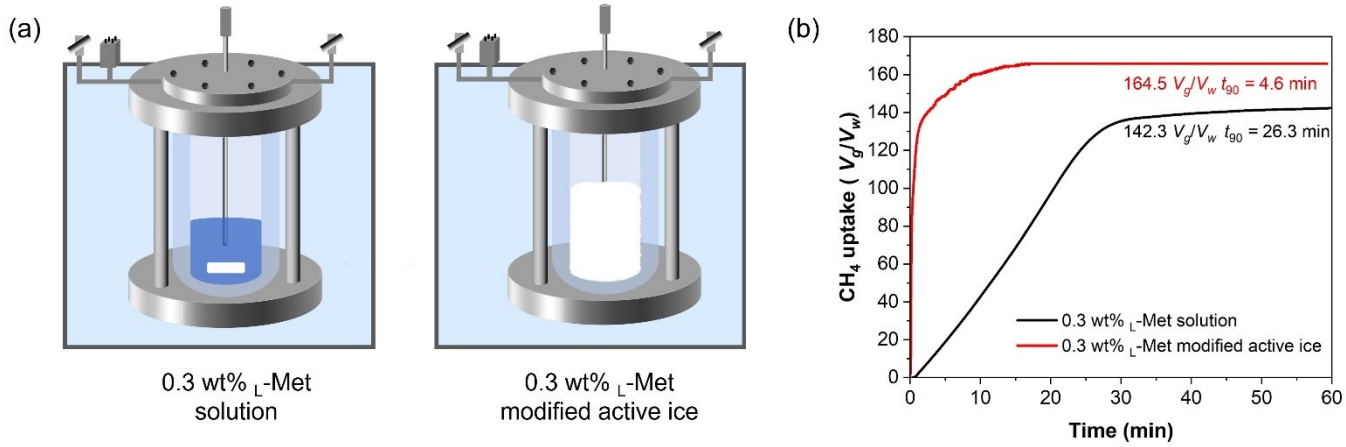

Fig. S27. (a) Schematic of CH_4 hydrate formation from 0.3 wt% $_L$-Met solution and 0.3 wt% $_L$-Met modified active ice; (b) Comparison of CH_4 uptake profile and t_{90} (time required to achieve 90% final CH_4 uptake) during CH_4 hydrate formation from 0.3 wt% $_L$-Met solution and 0.3 wt% $_L$-Met modified active ice at P = 6 MPa and T = 272.7 K.

(3) 0.3 wt% $_L$-Met modified active ice was formed at 273.2 K vs. 0.3 wt% $_L$-Met modified active ice was formed at 272.7 K: We also evaluated the necessity of a robust physical skeleton by preparing $_L$-Met modified active ice at a slightly higher temperature (273.2 K). As shown in Fig. S29, the CH_4 uptake decreased to 125.5 V_g/V_w (a 23.7% drop compared to the 272.7 K), and t_{90} shortened to 2.9 min. Although the growth rate was faster, the significantly reduced CH_4 storage capacity suggests that the active ice skeleton may be compromised, possibly due to partial melting of the ice matrix. Further experiments will be designed in future work to clarify the underlying mechanism.

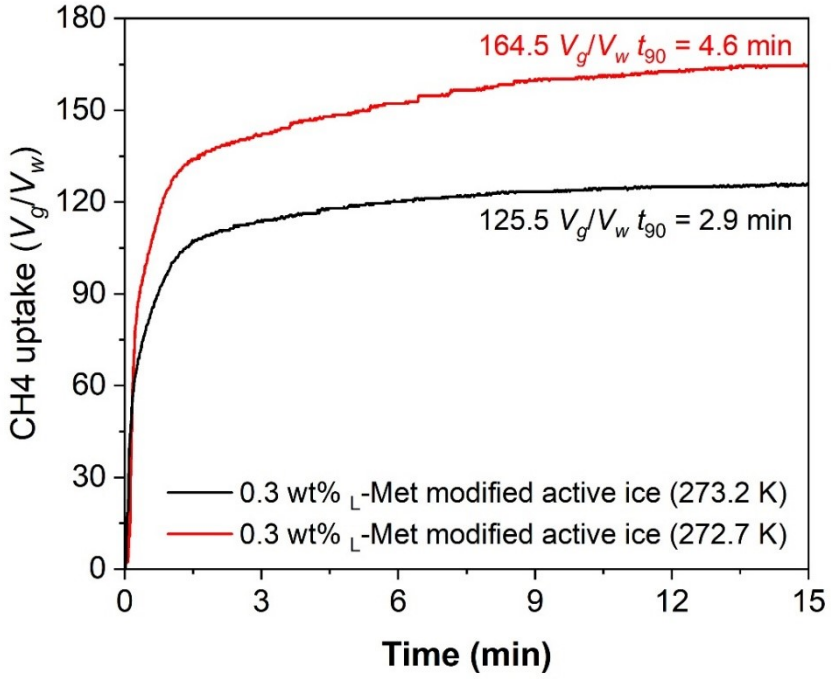

Fig. S28. Comparison of CH_4 uptake profile and t_{90} (time required to achieve 90% final CH_4 uptake) during CH_4 hydrate formation from 0.3 wt% $_L$-Met modified active ice at T = 273.2 K and T = 272.7 K under initial pressure of 6 MPa.

Section 4. Microscopic characterization of $_L$-Met solution and active ice

4.1 Measurement of contact angle and surface tension of $_L$-Met solutions at different concentrations

We measured the surface tension using the Wilhelmy plate method with a KRÜSS K11 tensiometer. With increasing $_L$-Met concentration, the surface tension slightly decreases, but the overall change is not significant. Specifically, it decreases from 72.97 mN/m for pure water to 71.93 mN/m at 3.0 wt% (see Fig. S29). We also measured the contact angle between quartz glass and $_L$-Met solutions of at different concentrations with a KRÜSS DSA25 drop shape analyzer. The results shown in Fig. S31. The results indicate that the contact angle decreases from 37.3° for pure water to 33.4° at 0.03 wt% $_L$-Met, then drops more significantly to 31.8° at 0.3 wt% and 30.6° at 3.0 wt% $_L$-Met. This trend suggests that higher $_L$-Met concentrations enhance the hydrophilicity of the surface.

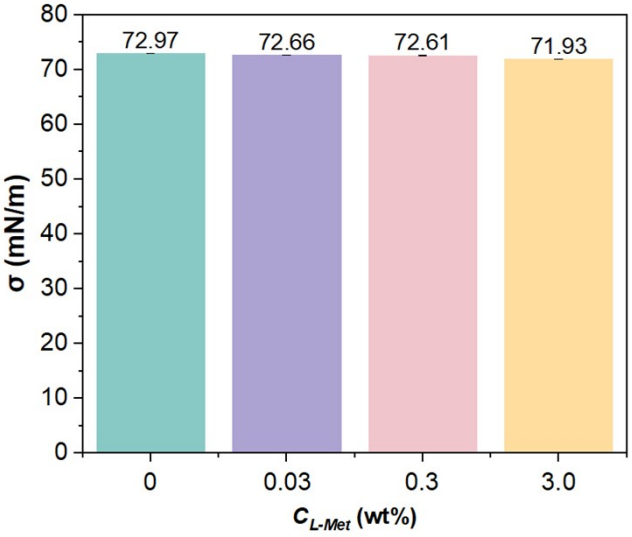

Fig. S29. Surface tension of L-Met solutions at different concentrations measured by the Wilhelmy plate method.

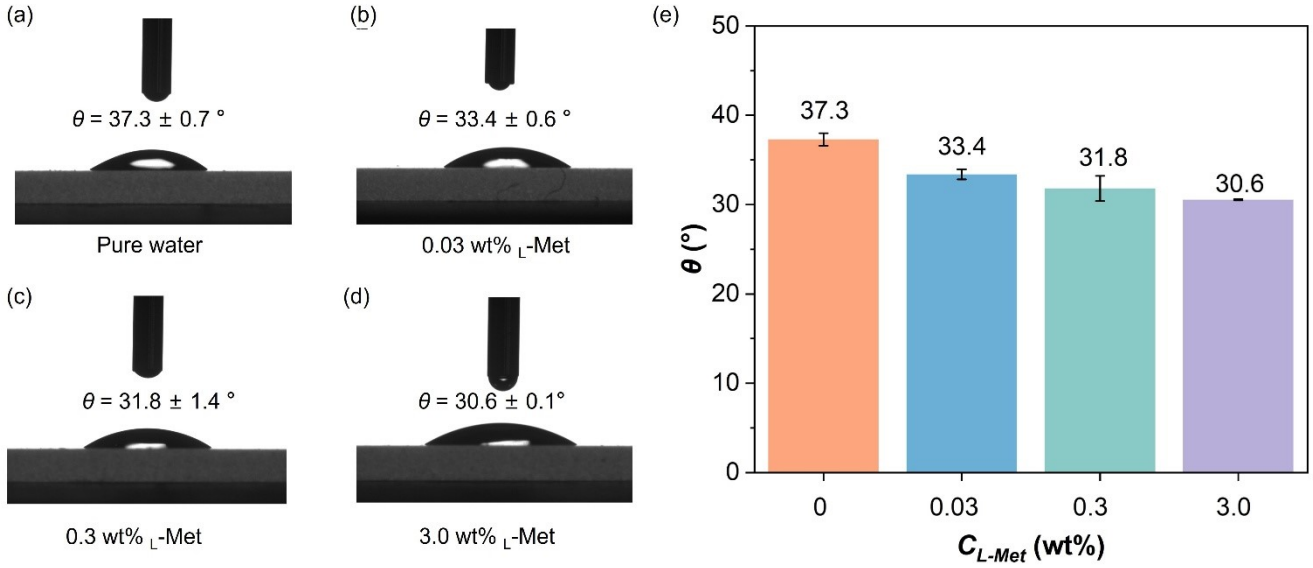

Fig. S30. Contact angle measurements of L-Met solutions on quartz glass: (a) 0 wt%, (b) 0.03 wt%, (c) 0.3 wt%, and (d) 3.0 wt%. (e) Comparison of contact angles for all concentrations.

By supplementing these surface tension and contact angle measurements, it is evident that the addition of L-Met alters the interfacial properties of the system, enhancing surface wettability and slightly lowering surface tension. However, the observed trends do not show a linear or monotonic correlation with CH_4 hydrate formation kinetics. Although such changes in interfacial properties may potentially facilitate hydrate nucleation and growth, their role in controlling the kinetic behavior appears to be limited in the active ice system investigated in this study.

4.2 Cryo-SEM characterization of active ice formed with different Met concentrations

To gain a deeper understanding of the modifying effect of $_{L}$-Met on the active ice surface and to quantitatively characterize its structural characteristics, cryogenic scanning electron microscopy (cryo-SEM) was employed. The cryo-SEM images representing the 0.3 wt% $_{L}$-Met modified active ice displays an overall well-connected porous network, featuring large and open pores on the surface (see Fig. S31), corresponding to a calculated total pore fraction of 22.1% (see Fig. S32). In contrast, the ryo-SEM images representing the higher concentration of 3.0 wt% $_{L}$-Met shows a different morphology where the structure has become less porous, evidenced by a reduced total pore fraction of 16.1% compared to the 0.3 wt% sample.

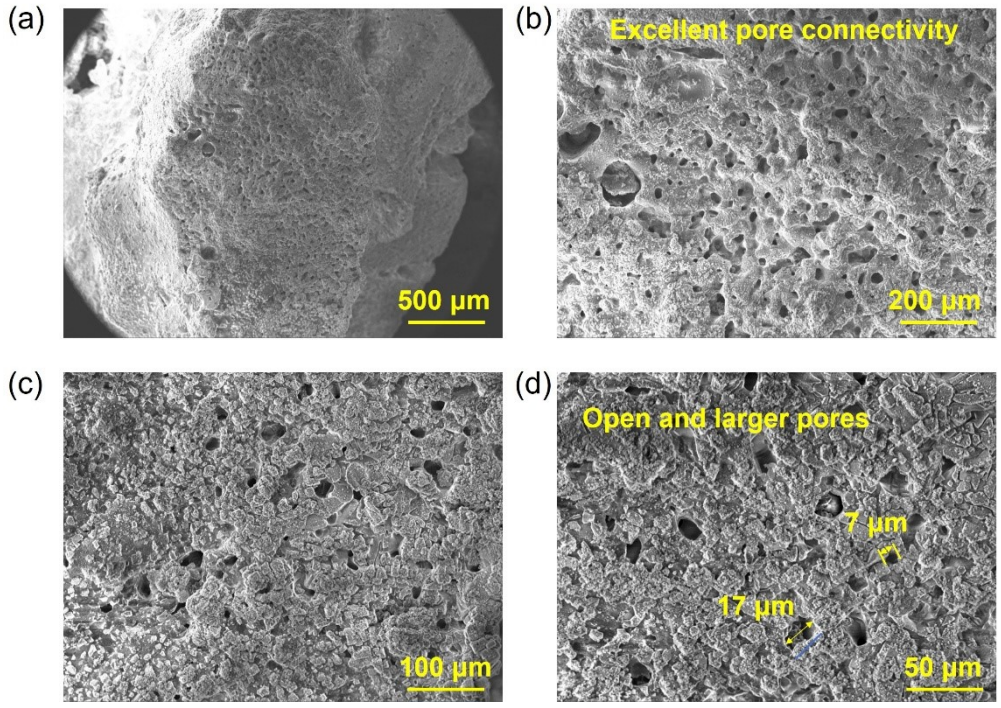

Fig. S31. Cryogenic scanning electron microscopy (Cryo-SEM) images of optimal 0.3 wt% $_{L}$-Met modified active ice at different magnifications: (a) overview showing excellent pore connectivity (500 µm); (b) intermediate view of the pore network (100 µm); (c)-(d) high-magnification views of open and larger pores (50-100µm).

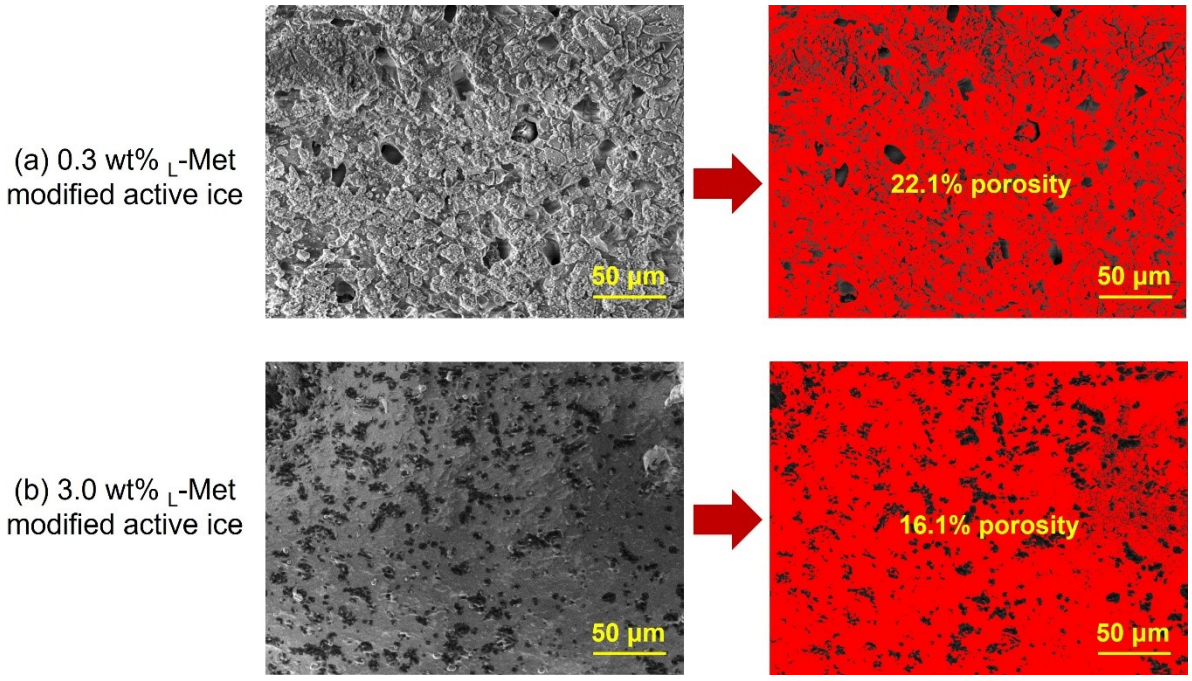

Fig. S32. Cryogenic scanning electron microscopy (Cryo-SEM) images and corresponding porosity analysis of active ice samples: (a) 0.3 wt% $_L$-Met modified active ice; (b) 3.0 wt% $_L$-Met modified active ice.

Section 5. Economic assessment based on experimental CH_4 storage capacity and kinetic promoter dosage

To rigorously evaluate the industrial feasibility, we further performed a quantitative economic analysis. We calculated the specific reagent cost required to produce 100 kg of methane hydrate based on the actual gas storage capacities (n_g) and optimal dosages obtained in our experiments. The calculation follows four steps: (i) determining the gas-liquid mass ratio (m_g/m_w) based on uptake (V_g/V_w):

$$\frac{m_g}{m_w} = \frac{n_g \times 16}{22.4 \times 1000} \tag{6}$$

where m_g/m_w represents the mass of CH_4 gas stored per unit mass of water, n_g represents the volume of CH_4 phase per volume of water.

(ii) calculating the required solution mass:

$$m_s = \frac{100}{1 + \frac{m_g}{m_w}} \tag{7}$$

where m_s represents the required mass of the solution to produce 100 kg of CH_4 hydrate.

(iii) calculating the amount of reagent needed based on the solution mass and concentration

$$m_p = m_s \times C \tag{8}$$

where m_p represents the mass of the kinetic promoter needed based on the solution mass and experimental dosage (C).

(iv) deriving the total reagent cost based on current market prices (CNY/g)

$$c_t = m_p \times p_u \tag{9}$$

where p_u represents the unit market price of the kinetic promoter.

The detailed results are presented in Table S6. When comparing with SDS modified active ice, although SDS exhibits the lowest raw material cost (8.90 CNY per 100 kg CH_4 hydrate) due to its extremely low dosage, this apparent economic advantage is largely offset by substantial environmental and safety liabilities. Specifically, SDS introduces toxicity risks and severe foaming, which in an industrial setting require additional wastewater treatment and safety management, thereby increasing the overall operational burden (see Table S7 and Fig. S26).

In contrast, producing 100 kg of hydrate using $_{\text{L}}$-Met modified active ice costs approximately 65.61 CNY, which is slightly higher than SDS in terms of raw material. Moreover, compared to another amino acid promoter, $_{\text{L}}$-Trp, which costs 98.46 CNY per 100 kg CH_4 hydrate, $_{\text{L}}$-Met offers a 33% cost reduction while maintaining a high storage capacity (156.05 V_g/V_w). Therefore, $_{\text{L}}$-Met provides a critical advantage which combines high economic viability with environmental safety, eliminating the hidden compliance and treatment costs associated with SDS, and offers a truly green and industrially acceptable solution.

In conclusion, L-Met successfully balances high performance and environmental safety with a low cost that is acceptable for industrial scaling, making it a superior green alternative. We also have thoroughly updated the literature review and added several representative recent works to better reflect key developments in this field. Additionally, we have carefully checked and standardized the citation format throughout the manuscript to ensure consistency and adherence to journal guidelines.

Table S6. Comparison of physicochemical properties, toxicity, and cost for different kinetic promoters.

Promoter	CH_4 Uptake (V_g/V_w)	Concentration (wt%)	Unit Price ($/g)	Calculated solution mass (kg)	Promoter mass required (g)	Total promoter cost ($/100kg CH_4 hydrate)	Ref.
SDS	185.00	0.06	0.024	88.34	53	1.27	Xiao et al.[8]
L-Trp	146.56	0.30	0.052	90.50	272	14.06	Zhang et al.[9]
L-Met	156.05	0.30	0.035	90.01	270	9.37	This study

Table S7. Comparison of physicochemical properties, toxicity, and cost for different kinetic promoters.

Promoter	Density (g/cm^3)	Boiling point (K)	Melting point (K)	Median lethal dose (LD_{50}) in rats (mg/kg)	Saturation solubility in water (wt%)	Skin Irritation	Aquatic toxicity	Biodegradability	Synthesis Method	Cost ($/g)
SDS	1.03	478	479	1288	15.0	Strong irritation	Toxic	Biodegradable but causes foam pollution	Fatty acid sulfation	0.024
$_{L}$-Trp	1.34	562	550	＞5000	1.1	N.A.	No clear toxicity	Easily biodegradable	Fermentation of serine and indole using wild-type or genetically modified bacteria	0.052
$_{L}$-Met	1.34	607.1	547	＞5000	3.4	N.A.	No clear toxicity	Easily biodegradable	Direct synthesis via fermentation with corynebacterium glutamicum	0.035

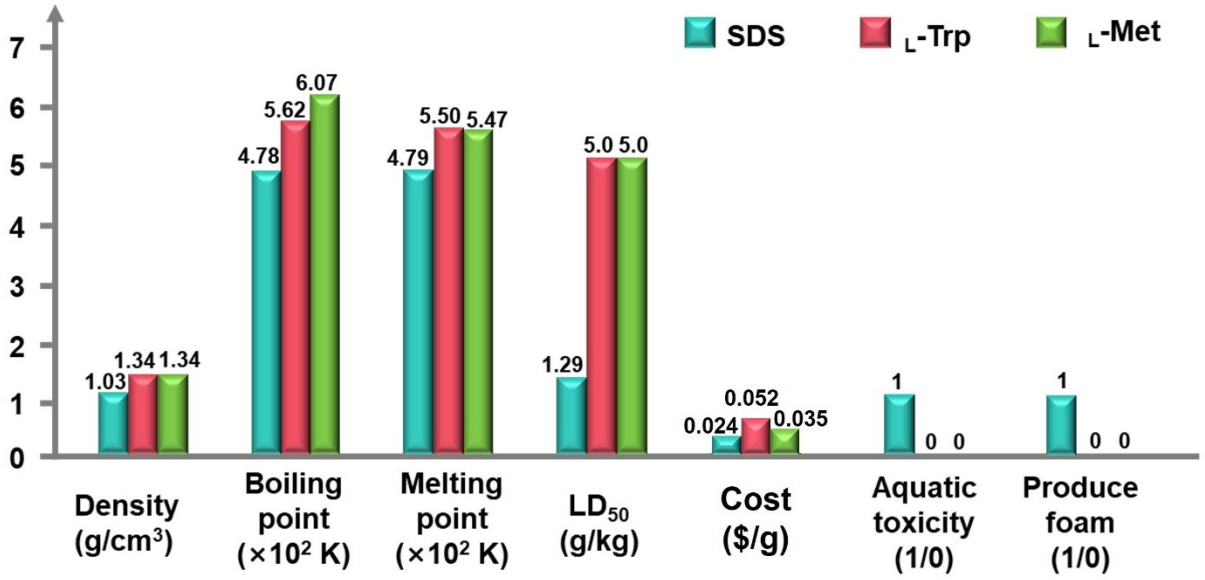

Fig. S33. Comprehensive evaluation of different kinetic promoters (SDS, L-Trp, and L-Met) based on physicochemical properties, economic cost, and environmental safety.

Section 6. Videos of morphology evolution during L-Met modified active ice synthesis and ultra-rapid CH_4 hydrate formation kinetics

Video SV1: A video of the morphology evolution for CH_4 hydrate formation from 0.3 wt% L-Met solution at P = 6.0 MPa, T = 277.2 K (1st formation stage) and subsequent T = 272.7 K (2nd formation stage).

Video SV2: A video of the morphology evolution for CH_4 hydrate dissociation to form 0.3 wt% L-Met modified active ice at P = 0.1 MPa and T = 272.7 K.

Video SV3: A video of the morphology evolution for CH_4 hydrate formation from 0.3 wt% L-Met modified active ice at P = 6.0 MPa and T = 272.7 K.

Reference

1 H. S. Truong-Lam, S. J. Cho and J. D. Lee, *Appl. Energy*, 2019, **255**, 113834.

2 K.-F. Yan, J.-Y. Zhao, H. Chen, X.-S. Li, C.-G. Xu, Z.-Y. Chen, Y. Zhang, Y. Wang, J.-C. Feng and Y.-S. Yu, *Chem. Eng. Sci.*, 2023, **276**, 118829.

3 K. Jeenmuang, P. Pornaroontham, M. Fahed Qureshi, P. Linga and P. Rangsunvigit, *Chem. Eng. J.*, 2024, **479**, 147691.

4 J. Sun, X. Liu, C. Xu, P. Bian and Z. Yin, *Chem. Eng. J.*, 2025, **521**, 166697.

5 J. Li, W. Zhao, P. Xiao, H. Zhang, K. Liu, M. Qi, B. Yang, G. Chen and C. Sun, *Chem. Eng. Sci.*, 2025, **305**, 121200.

6 T. Nakamura, T. Makino, T. Sugahara and K. Ohgaki, *Chem. Eng. Sci.*, 2003, **58**, 269–273.

7 X. Shen, Y. Li, Y. Li, L. Shen, N. Maeda, Y. Zhang, H. Wang and X. Wang, *ACS Sustain. Chem. Eng.*, 2023, **11**, 8774–8785.

8 P. Xiao, J.-J. Li, W. Chen, W.-X. Pang, X.-W. Peng, Y. Xie, X.-H. Wang, C. Deng, C.-Y. Sun, B. Liu, Y.-J. Zhu, Y.-L. Peng, P. Linga and G.-J. Chen, *Nat. Commun.*, 2023, **14**, 8068.

9 Y. Zhang, Y. Ma, K. Jeenmuang, G. Vishwakarma, C.-Y. Sun, G.-J. Chen and P. Linga, *Nat. Commun.*, 2025, **16**, 8670.